



Application of Urban Solar Power Prediction on Controlling a Stand-alone PV-Battery Hybrid System

Author:

Chen, Zihao

Publication Date:

2017

DOI:

<https://doi.org/10.26190/unsworks/19923>

License:

<https://creativecommons.org/licenses/by-nc-nd/3.0/au/>

Link to license to see what you are allowed to do with this resource.

Downloaded from <http://hdl.handle.net/1959.4/58651> in <https://unsworks.unsw.edu.au> on 2024-05-05

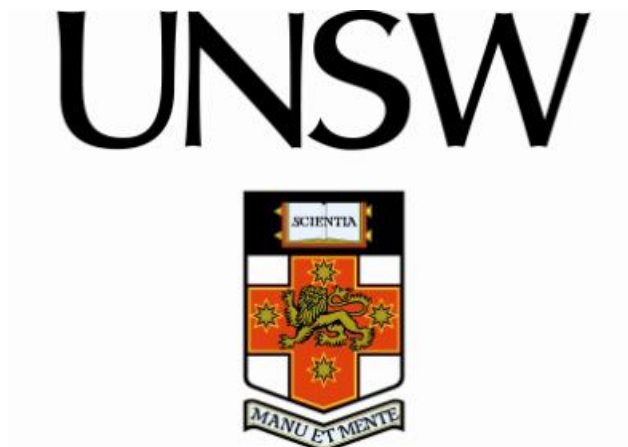
Application of Urban Solar Power Prediction on Controlling a Stand-alone PV-Battery Hybrid System

Zihao Chen

**A thesis submitted in fulfilment of the requirements for the
degree of Master of Engineering (Research)**

Supervisor: A/Prof. Hemanshu R. Pota
(The University of New South Wales, Canberra)

Co Supervisor: Dr. Alberto Troccoli
(The Commonwealth Scientific and Industrial Research Organisation, Canberra)



School of Engineering and Information Technology

The University of New South Wales, Canberra

March, 2017

Contents

List of Tables.....	III
List of Figures	II
Abbreviations and Acronyms.....	V
List of Publication	VI
ACKNOWLEDGEMENT	VII
ABSTRACT	IX
Chapter 1 Introduction	1
1.1 Solar prediction using nearby stations.....	4
1.2 Statistical prediction methods	6
1.3 Controlling method for solar panels and battery banks.....	7
1.4 Outline	10
Chapter 2 Solar Irradiance Prediction	11
2.1 Observations and Methodology.....	11
2.1.1 Observations	11
2.1.2 Prediction Methods	12
2.1.2.1 Multi-linear Model.....	12
2.1.2.2 Random Forest model	14
2.1.2.3 Persistence.....	16
2.1.3 Prediction set up and Assessment.....	17
2.2 Relative importance of predictors	19
2.3 Relative importance of monitoring stations	27
2.4 Conversion of GHI prediction into power prediction	31
2.4.1 Dependency of power prediction on sky conditions.....	37

Chapter 3 Test Platform and Control for the Integrated PV Solar and Battery System..	41
3.1 Test System	41
3.2 System Modelling.....	42
3.2.1 Modelling of the unidirectional DC-DC converter.....	42
3.2.2 Modelling of the Bidirectional DC-DC Converter	44
3.3 Controlling Design for the Integrated PV Solar and Battery System.....	52
3.3.1 Controlling Design for the Unidirectional DC-DC Converter	53
3.3.2 Controlling Design for the Bidirectional DC-DC Converter.....	56
Chapter 4 Results	67
Chapter 5 Summary and discussion	75
5.1 Summary and prospective of the prediction method.....	75
5.2 Summary and prospective of the control algorithm	78
References	81

List of Tables

Table 2-1 Best options for GHI prediction	24
Table 2-2 Best options for power prediction.	27
Table 2-3 Tilt and orientation angles of the three PV systems.	32
Table 3-1 The voltage threshold for different converter states	58
Table 3-2 Different situation numbers for different modes	58
Table 3-3 The anticipating actions of the IGBT in a prediction horizon and its corresponding cost function values	66
Table 4-1 The solar irradiance measurement data from 31-01-2017 13:03:29 to 31-01-2017 13:03:50	68

List of Figures

Figure 2-1 Map of Canberra with the position and names of our five monitoring stations. Highlighted with circles are the three stations used for our solar forecasting algorithms, with Namadgi School taken as the target station	12
Figure 2-2 Examples of horizon time.....	14
Figure 2-3 Clear-sky index Distribution at Namadgi School for summer (top) and winter (bottom) and for both training period (grey bars) and prediction period (black bars)....	19
Figure 2-4 rMAE of GHI Prediction. (a) Predictors: GHI only; (b) Predictors: GHI, Air Pressure, Absolute Humidity; (c) Predictors: GHI, Air Temperature, Absolute Humidity; (d) Predictors: GHI, Air Temperature, Air Pressure (Dashed lines show results for summer, solid lines for winter).	23
Figure 2-5 rMAE of Power Prediction. (a) Predictors: Global Irradiance on Tilted Surface (SP-Solar), PV panel temperature, Absolute Humidity; (b) Predictors: GHI, Air Temperature, Absolute Humidity. Dashed lines show results for summer, solid lines for winter.....	26
Figure 2-6 rMAE of GHI predictions using data from different stations (a) in summer (Method: Random Forest; Predictors: GHI, Air Pressure, Absolute Humidity); (b) in winter (Method: Multi-Linear; Predictors: GHI, Air Pressure, Absolute Humidity).	30
Figure 2-7 Diffuse Fraction versus clear-sky index for Black Mountain station. The red line is the fitted line using the loess R function.	32
Figure 2-8 rMAE of modified Power predictions based on the conversion presented in Section 5 and using data from different stations (a) in summer (Method: Random Forest; Predictors: SP-Solar, PV panel temperature, Absolute Humidity); (b) in winter (Method: Multi-Linear; Predictors: SP-Solar, PV panel temperature, Absolute Humidity).	36

Figure 2-9 rMAE of Power prediction under clear sky and non-clear sky conditions (station used: Black Mountain and Wombat Hill; Predictors: SP-Solar, PV panel temperature, Absolute Humidity). (a) Summer, with local data; (b) Summer, without local data; (c) Winter, with local data; (d) Winter, without local data	40
Figure 3-1 System topology of the PV-Battery hybrid system	42
Figure 3-2 (a) The topology of the PV panels, unidirectional DC-DC converter and DC bus; (b) The equivalent circuit	43
Figure 3-3 The system circuit when $S_3=1$	43
Figure 3-4 The system circuit when $S_3=1$	43
Figure 3-5 The topology of the battery, bidirectional DC-DC converter and DC bus....	45
Figure 3-6 The equivalent circuit of buck mode	45
Figure 3-7 The equivalent circuit when $S_1 = 1$ (buck mode)	46
Figure 3-8 The equivalent circuit when $S_1 = 0$ (buck mode)	47
Figure 3-9 The logic of conduction mode selection	48
Figure 3-10 The equivalent circuit of boost mode	49
Figure 3-11 The equivalent circuit when $S_2 = 1$ (boost mode)	50
Figure 3-12 The equivalent circuit when $S_2 = 0$ (boost mode)	51
Figure 3-13 P-V curve of BP Solar SX3190 under different solar irradiance	54
Figure 3-14 The logic of the MPPT algorithm.....	56
Figure 3-15 The simplified battery model	62
Figure 3-16 The possible values sequence of a single IGBT in buck or boost mode (0-off; 1-on)	65
Figure 4-1 The solar irradiance measurement of Black Mountain site from 31-01-2017 13:03:00 to 31-01-2017 13:03:59	67
Figure 4-2 The change in the measurement and prediction during the selected period..	68

Figure 4-3 The logic of the operation69

Figure 4-4 The voltage of DC bus (prediction horizon time: 1s)..... 70

Figure 4-5 The values of control signals (S1 and S2) (prediction horizon time: 1s)..... 71

Figure 4-6 The current and voltage of the battery (prediction horizon time: 1s)..... 72

Figure 4-7 The power change of pv panels, load and battery (prediction horizon time: 1s)
..... 72

Figure 4-8 The voltage of DC bus (prediction horizon time: 5s)..... 73

Figure 4-9 The values of control signals (S1 and S2) (prediction horizon time: 5s)..... 73

Figure 4-10 The current and voltage of the battery (prediction horizon time: 5s)..... 74

Figure 4-11 The power change of PV panels, load and battery (prediction horizon time:
5s)..... 74

Abbreviations and Acronyms

PV	Photovoltaic
GHI	Global Horizontal Irradiance
rMAE	Relative Mean Absolute Error
MPPT	Maximum Power Point Tracking
MPC	Model Predictive Control
ANN	Artificial Neural Network
ARIMA	Autoregressive Integrated Moving Average
DNI	Direct Normal Irradiance
Diff	Diffuse Horizontal Irradiance
TDNN	Time Delay Neural Network
AR(2)	Autoregressive Model of Order 2
CARDS	Coupled Auto Regressive Dynamic System
NWS	National Weather Service
SVM	Support Vector Machine
P&O	Perturb and Observe
SOC	State of Charge
ACT	Australian Capital Territory
DF	Diffuse Fraction
IGBT	Insulated-Gate Bipolar Transistor
MOSFET	Metal–Oxide–Semiconductor Field-Effect Transistor
CCM	Continuous Conduction Mode
DCM	Discrete Conduction Mode

List of Publication

Zihao Chen, and Alberto Troccoli. "Urban solar irradiance and power prediction from nearby stations." *Meteorologische Zeitschrift* (2015). DOI: 10.1127/metz/2016/0725.

ACKNOWLEDGEMENT

I would like to express my deepest appreciation to all those who have provided me help on my study and the completion of this thesis.

My special thanks go to my supervisor, A/Prof Hemanshu Pota and Dr Alberto Troccoli for their huge and constant support, guidance and encouragement through my study at UNSW Canberra. Despite his busy schedule, A/Prof Pota always spared time for meeting when I needed. His great creativity in research and sense of humour always inspire me of new thinking and lead me out of frustrations. Dr Troccoli, who is of great patience and wisdom, guided me into the field of meteorology. His positive attitude and outstanding academic ability have given me power to overcome difficulties in my study. They are two of the most excellent persons I have ever met in my life and without their help, this thesis could not have been completed.

I would like to thank Mr Pablo Rozas Larraondo, Mr Mark Kitchen, Dr Jing Huang, Mr Robert Davy, Mr Chris Price and all other staffs who have provided me help in Commonwealth Scientific and Industrial Research Organisation. I am also grateful to Mr Wei Lu, Dr Chengdi Xiang, Dr Shan Ma and Mr Liang Wu for the valued and valuable advice and all the great moments they have brought to me. Last but not the least, I treasure the love from my parents, my grandmother and my grandfather who is now living in the heaven. I would like to take this chance to express my sincere love to them.

Finally, the measurement data used in this study have been collected and maintained by the Weather and Energy Research Unit of Commonwealth Scientific and Industrial Re-

search Organisation (CSIRO, <http://weru.csiro.au>). This work was supported by the Australian Solar Energy Forecasting System project, co-funded by CSIRO and the Australian Renewable Energy Agency (ARENA).

ABSTRACT

With the proliferation of small-scale solar PV installations, global horizontal irradiance (GHI) and power predictions are becoming critical elements in the integration of PV generation into the grid. This thesis considers short-term prediction, from minutes to hours, based on historical meteorological measurement data from weather and power monitoring stations located in the Canberra (Australia) region. The specific objective of this study is to produce accurate forecasts for (a generic) target station using a minimal amount of observations from nearby stations. Thus, although a large number of weather and power variables were collected and used for developing and testing the prediction algorithms, the ultimate aim is to rely on a few predictors, mainly meteorologically based. This will allow the identification of critical instruments which would need to be installed in order to provide satisfactory PV power predictions while limiting capital and operating costs of monitoring. Relative mean absolute error (rMAE) is used to indicate prediction performance. Three statistical methods are tested for two different seasons, winter and summer. The relative importance of predictors and stations is assessed. A conversion from GHI to global irradiance on tilted surfaces, by means of simple geometry arguments and notion of irradiance components at a nearby site, is also introduced and tested. Finally, the prediction accuracy is categorised according to different clear-sky indexes. Results show that when the clear-sky index exceeds 0.9 (near-to-cloudless conditions), the prediction performance is distinctly better than at lower clear-sky indices which are under 0.9, by at least 0.05 and 0.2 in terms of rMAE in summer and winter, respectively. The second contribution of this thesis is a standalone PV-Battery hybrid system and the solar irradiance anticipation is used as simulation input to PV panels. There are two converters in

the hybrid model. The unidirectional DC-DC converter, which is linked between PV panels and DC bus for power supply, works under maximum power point tracking (MPPT) mode, while the other, the bidirectional DC-DC converter located between battery banks and DC bus, operates under a model predictive control (MPC) algorithm. By charging and discharging the battery, the voltage of the DC bus can be kept in a certain range to meet the load requirement.

Chapter 1 Introduction

Electricity, as the most effective and convenient form of energy, is indispensable in almost all activities of modern times. Conventional generators, the mechanical energy of which normally comes from combusting coal, oil or natural gas, have dominated the electric power generation for a long time. As industrialization extends to rural area and populations grow, the need for more and more electricity becomes urgent. However, during the last decades, human beings have witnessed the environmental degradation including the pollutant emissions from fossil fuel combustion such as SO₂, NO_x, particulate and CO₂ [6]. With the conflict between the growing electricity demand and the environmental benefits, renewable energy is expected to be a potential solution as it is abundant, eco-friendly and widely distributed. Among renewable resources, wind power has experienced the most development over the last few decades in the United States. Solar energy, lagging behind though, is expected to get close to and even take over the dominating place of wind [15]. The advantages of solar energy compared to other renewable resources are listed below:

1. Unlike some other renewable resources confined to particular geographical area, say tidal and geothermal, solar power is accessible and available in every corner of the world.
2. Solar power can be used easily on small scales without connecting to the power grid. It is therefore an ideal energy source for increasing regional energy independence and extending electrification to rural and remote areas.

3. The ‘plug and play’ nature and high mobility of solar panels make solar power systems easier to be deployed than any other energy systems. So it is an ideal energy source in urgent contexts like after-disaster rescue and reconstruction.
4. Due to the intensive attention and resource put into sun power research, the efficiency of solar panels is getting increasingly high while the cost for per megawatt installation is becoming lower and lower [37].

Installations of residential solar photovoltaic (PV) panels have grown rapidly in several countries, mainly encouraged by government incentives, increasing energy prices and reductions in the cost of solar power. Latest estimates indicate about 4 GW in installed small scale PV power for Australia. With progressively lower PV production costs and improving system quality and reliability, growth in installations in the near future is projected to be even stronger (AEMO 2012).

Despite all the advantages solar power may have, the drawback, which is of the intermittent nature as other clean energy sources may have, prevents it from proliferating fast. The upgoing penetration of solar energy poses a large operational challenge to existing transmission grid such as additional ramping, power system stability and so on. For example, a partly cloudy day may lead to a high frequency of ups and downs in terms of solar power output. This may make the voltage or frequency of a weak power system unstable, or even worse, cause a blackout. Hourly and even subhourly prediction of solar radiation and PV-produced power at the residential and business level is therefore key to alleviate the problems related to intermittency. To be more exact, based on forecasting result, electric energy storage, such as batteries can be dispatched in advance to compensate power deficit, absorb power redundancy and allow a smoother integration of power into the electricity grid. In fact, most of the controlling algorithms need a reference value

to follow which is the prediction power/current difference between solar generation and power consumption. For power systems, the prediction from the consumer side is based on factors like location, seasonal effect, the electricity using habits of local citizens and so on. It is usually accurate enough. However, the high-end precise projection for the generation side of renewable plants still remains to be sought. Once they are ready, the reference value will be available for power dispatching.

Ideally, one would collect all of the relevant variables from each individual installation to accurately describe the specific system parameters and hence attempt a detailed solar power prediction for each system. However, this would clearly be a very expensive, time consuming and essentially impractical approach since PV installations are characterized by a variety of features: i) PV technology, ii) inverter type and technology, iii) panel orientation (including accounting for tracking devices), iv) amount of shading (which can depend on variables such as solar zenith angle, but also on the changing nature of obstructions), v) efficiency of the PV panels (dependent on the type of installations, whether free standing or roof integrated systems, as well as on weather conditions, such as air temperature and wind speed).

It is apparent therefore that a deterministic approach to urban or regional PV power forecasting is impractical. Practical approaches to predicting solar power at increasing level of approximation are therefore sought. Such approaches by necessity will have to consider PV system aggregation to differing degrees. Sometimes these approaches are called upscaling: prediction is derived for a small sample of PV systems, which is then used to infer the behavior of analogous PV systems over a broader area. An increasing number of attempts at predicting solar power at urban and/or regional level have been made. Amongst these, the most notable was the work of Lorenz et al. [24] and Lorenz et al. [26].

They modelled PV installations from a small region in Germany to derive solar power predictions over most of Germany, making use of solar irradiance forecasts from a numerical weather prediction model and PV installation information available through power authorities and/or power companies. Although specific information of each individual system was not required, this method attempted detailed descriptions of PV system characteristics such as the efficiency of PV generators or the module temperature, which were derived by means of parameterized models. The temporal horizon of their prediction, essentially determined by the irradiance forecast, was from 1 hour to 3 days ahead. It was worth noting also that a similar technique had also been used in wind power forecast, too [9].

1.1 Solar prediction using nearby stations

In the absence of solar irradiance, power predictions could be produced by the sole use of power output, measured by a sample of systems (e.g. from <http://pvoutput.org>, a public web site with user submitted power output data). These methods rely on spatial and temporal correlation of neighbouring PV systems. Golnas et al. [12] proposed a method of estimating the energy output of a certain PV system by using information from neighbouring systems like historical performance correlation and inter-system distance. In their research, the weekly and monthly energy generation from 55 systems located in New Jersey was predicted. Results indicated that the method was satisfactory for long lead-time cases: the success rate for weekly prediction was more than 91% with a 10% accuracy threshold while for monthly prediction, it was more than 96% with the same accuracy threshold. Lonij and Jayadevan [23] used 80 residential rooftop PV systems distributed over a 50 km x 50 km area as irradiance sensors. Their approach was based on the system performance under clear skies. The forecast performance under all sky conditions

relied heavily on cloud velocity estimation. They also found that the RMS error could be improved if there was a better measurement or estimation of cloud velocity. Recently, Engerer and Mills [8] developed a clear-sky index for PV power output estimation. By using this clear-sky index, the performance of nearby PV systems could be predicted accurately according to tests carried out using power output data (with time resolution of 5 minutes) from five residential PV systems in Canberra.

In this work, we start from the underlying assumption that, because the ultimate driver of PV systems and their outputs is global irradiance, accurate meteorological observations are key to accurate power predictions. At the same time, and with the view to limit the amount and cost of instrumentation required for accurate forecasts, we also assess the type and number of meteorological observations required to achieve accurate forecasts. The irradiance forecasts are then used to produce power forecasts for a target (generic) system.

This work relies on a number of high-frequency monitoring stations installed, and regularly maintained, around Canberra. Specifically, we use measurements from two stations to produce forecasts for a third target station, for which we have all measurements. Where the geometry of the PV system is known, as in our case, we derive the global irradiance on the PV plane by means of statistical relationship between the three irradiance components (global, diffuse and direct). In the absence of PV system specifications, one would need to make standard assumptions about system performance, tilt and orientation angles.

The prediction lead (or horizon) time extends from 5 minute to 3 hours ahead. Such time frames are particularly useful for regulation reserves, and enhanced system reliability and security and, potentially, for load shifting, at the high-end of this horizon time. At these

lead times, it is generally accepted that statistical techniques offer the most appropriate and practical approach [25] [35].

1.2 Statistical prediction methods

Some of the most common statistical methods used to compute solar radiation forecast includes regression analyses and machine learning [2] [34]. Machine learning methods, such as Artificial Neural Network (ANN) [7] [29] are widely used too. Yang et al. [39] proposed three ARIMA methods to predict global horizontal irradiance (GHI). The first method used historical GHI measurement to predict GHI. With the second one, GHI was decomposed into direct normal irradiance (DNI) and diffuse horizontal irradiance (Diff) before predicting DNI and Diff separately. Then GHI prediction was derived by combining Diff forecast and DNI forecast. The last method also took cloud cover into account and combined the predicted cloud effect (cloud transient was estimated by ARIMA method) with the solar zenith angle to forecast solar radiation (solar irradiance under different zenith angle and cloud cover was then predicted by a nonlinear regression method).

Linear and machine learning methods are also used in combination. For instance, Ji et al. [16] proposed an Autoregressive Moving Average (ARMA) and Time Delay Neural Network (TDNN) hybrid model for solar irradiance prediction. Huang et al. [14] proposed an AR(2) model to predict one hour ahead global solar irradiance. In their work, they also combined the AR(2) model with a resonating model to form a more accurate and reliable forecasting model which they called Coupled Auto Regressive Dynamic System (CARDS). Error analysis indicates that CARDS could effectively decrease the median absolute percentage error by 33.4%. Sharma et al. [36] collected both historical observational solar power data and the corresponding weather forecast data from National

Weather Service (NWS), which were then used for Support Vector Machine (SVM) training, to create a site-specific machine learning forecast model. Meanwhile, in that research, the linear least square was also tested and compared with the SVM model and a past-predicts-future model. Result showed that both the Support Vector Machine model and linear least square model outperformed the existing forecast-based model.

In this work we use two statistical methodologies, which we will inter-compare: a multi-linear model and a statistical learning machine model, called random forest. A modified persistence method is also used as a benchmark.

1.3 Controlling method for solar panels and battery banks

There is a lot of research focusing on solar irradiance prediction. The reasons may be because renewable energy is really difficult to be used or integrated into a power grid due to its intermittency nature. This is especially true for the most popular two, solar energy and wind energy. Besides a high-end prediction algorithm, in order to make solar energy possible to contribute to energy market, a reasonable and effective controlling strategy should also be considered as an indispensable factor.

As a power source in a circuit, solar panel arrays have much of a role to play in system operation. Therefore, a controlling scheme on the solar cell side is of extreme importance. In order to transfer solar irradiance to electricity in the most efficient way, Maximum Power Point Tracking, also known as MPPT, is the most commonly used algorithm for controlling PV panels' output. Many of the MPPT controllers are voltage-based and with Perturb-and-Observe (P&O) nature, which means that the sensing of different real-time parameters such as voltage and power output is required [1] [11]. Rather than using the P&O method, Rai et al. [32] proposed a machine learning based algorithm for maximum

power tracking. In this study, a three-layer feed forward perceptron neural network was trained and then used to predict the maximum power voltage and current under different meteorological conditions and variable load situations. There are a lot of other principles that could be used to determine the MPPT [10]. Of course, they have their own pros and cons which should be taken into account before choosing one from them.

Power storage is also crucial in a renewable energy system. Battery storage, as one of the most frequently used means of storing electric power, may be the most effective solution to the intermittency nature of the two popular renewable energy sources, wind and solar. In an isolated power system, it can fulfil peak shaving and improve the power quality [31] while in a grid-connected system, it can compensate the output fluctuation in order to make the output behaviour more similar to a conventional plant [20]. Liao et al. [21] proposed a power control method based on four different working situations for a standalone solar photovoltaic system with battery storage. In that study, the PV panels were linked with a 100V DC bus through a unidirectional (has three operating modes: Maximum Power Point Tracking (MPPT), Constant Voltage (CV) and Shut-down (SD)) DC-DC converter while the 48V battery banks were linked with the DC bus through a bidirectional one (has three operating modes: Boost, Buck and Shut-down (SD)). Such a model structure was straightforward and easy to be understood as PV systems always acted as a power source, but the battery storage, could be either power source or power load. According to battery and solar cell array voltages, and the charging and discharging current of battery, the working principle of the controller was divided into 4 modes which are basically related to the aims of extracting maximum power from PV panels if possible, protecting battery from over-charge or over-discharge, and trying to provide sufficient and stable power to the load. Using a similar electrical structure to Liao et al, Mahmood

et al. [28] proposed a multi-loop control strategy instead of using discrete state. The control algorithm contained two loops, one was for monitoring the State of Charge (SOC) of the battery, and the other one was for balancing the system power when the power produced from the PV system was far more than the power consumption from both battery and load. It was worth noting that the PV cells might operate at maximum power point or at some points with less power as a compromise to system power balancing requirement. This control scheme was then tested and verified on a 2kw prototype and it was proven that this scheme could work properly under some different situations such as load increasing or decreasing.

Model predictive control (MPC) has the potential to be used as a controlling method in a system where a renewable energy source is involved. Teleke et al. [38] proposed a MPC-based control method in a wind-battery hybrid power system. In this study, a simplified battery mathematical model was shown and with the model predictive control, a power output reference from battery banks was given and the gap between the real and reference values was set as the performance index. Results showed that the power of a wind farm could be dispatched on an hourly basis like a conventional generator. Also, by setting constraints of battery current and State of Charge (SOC) limit of battery in the MPC controller, the battery could be protected from problems like overcharging or undercharging which would effectively extend the lifetime of the battery system. Khalid et al. [18] also used MPC as a controlling solution for smoothing wind power output with battery storage. In addition, this research highlighted a wind prediction method. Such a forecast was based on the prediction of the wind vectors using the corresponding information from some

nearby stations. Once the target output was known, this improvement in wind power prediction would allow a more accurate reference power output value for the battery to keep track of and the battery could be effectively deployed in advance.

1.4 Outline

Section 2 shows the prediction part of this study. First, the observations and methodology used in this work is described. In addition, we study the relative importance of predictors amongst various observed meteorological and power variables. The relative importance of monitoring station locations used in the forecast algorithms is also investigated in this section. At the end of Section 2, we propose a simple empirical conversion method to produce solar irradiance on a tilted surface, which is then used to produce power forecasts. Results are also analyzed for clear and non-clear skies. In Section 3, a stand-alone PV-Battery model is proposed and the simplified circuit is presented, followed by the content of demonstrating how the unidirectional DC-DC converter and the bidirectional DC-DC converter are modelled. In this section, the MPPT algorithm and MPC algorithm for this hybrid system are also given. A case study based on different prediction result is shown in Section 4, where the circuit and control algorithm proposed in Section 3 is implemented. Section 5 offers a summary and a discussion about possible future improvements.

Chapter 2 Solar Irradiance Prediction

2.1 Observations and Methodology

2.1.1 Observations

Key to this work is the urban observation network based around Canberra, in the Australian Capital Territory (ACT). Such stations simultaneously monitor meteorological and electrical variables of co-located PV systems. Five stations are operating at present, and collect electrical variables such as current and voltage from which power is derived and meteorological variables such as global irradiance, both on horizontal and PV panel plane, PV panel temperature, air temperature, wind speed and direction, humidity, pressure and precipitation. All variables are logged at 1 second. However, in order to reduce the degrees of freedom of the prediction problem, 5-min averages are considered here.

Due to current constraints on data availability and quality, only three stations can be used for this study (see Figure 1). They are Black Mountain (geographical coordinates: 149.1E, 35.3S; elevation: 595m), Namadgi School (149.1E, 35.4S; 602m) and Wombat Hill (149.2E, 35.5S; 951m). Their relative distances as the crow flies are as follows: Black Mountain – Namadgi School 13 km, Black Mountain – Wombat Hill 29 km, Wombat Hill – Namadgi School 18 km. Given its location, Namadgi School, which is roughly located between Black Mountain and Wombat Hill, is selected as the target station in our forecasting experiments.

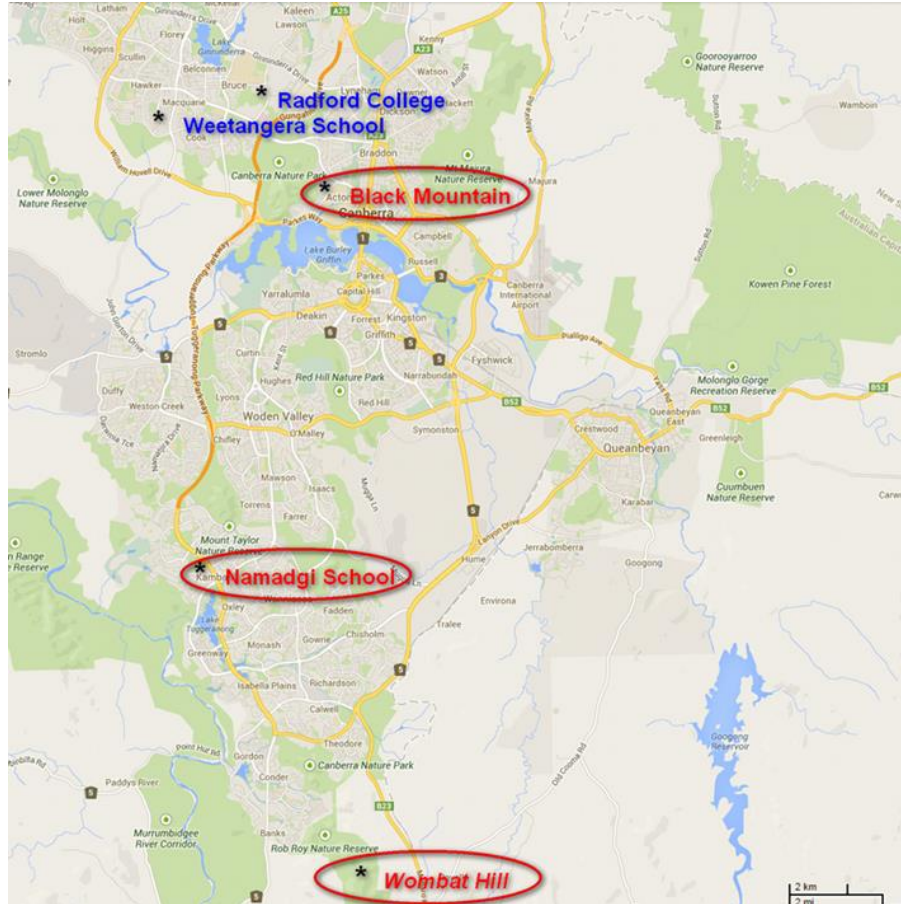


Figure 2-1 Map of Canberra with the position and names of our five monitoring stations. Highlighted with circles are the three stations used for our solar forecasting algorithms, with Namadgi School taken as the target station

2.1.2 Prediction Methods

Two statistical prediction models, multi linear and random forest, are evaluated in this work. They are assessed based on different predictors, seasons, and combination of ground stations. These two methods are benchmarked against a (modified) persistence method, which is described below.

2.1.2.1 Multi-linear Model

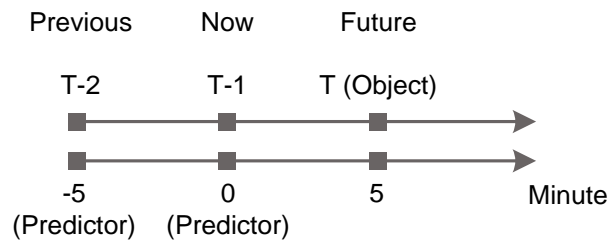
The multi-linear model used in this work is a linear method based on the AR(2) model. The following equation shows how solar power output prediction is obtained when solar power (P), solar irradiance (I) and panel temperature (T) are taken as predictors:

$$P_t = \alpha + \beta_1 P_{t-n} + \beta_2 P_{t-(n+1)} + \gamma_1 I_{t-n} + \gamma_2 I_{t-(n+1)} + \delta_1 T_{t-n} + \delta_2 T_{t-(n+1)} \quad (2-1)$$

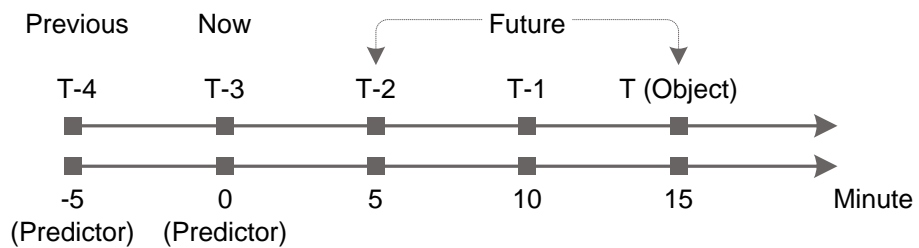
where 'n' is the time step. More specifically, 'n' is the ratio between the forecast horizon time (HT, in minutes, also called lead time) and the temporal resolution of the data (5 minutes in this case).

$$n = \frac{HT}{5} \quad (2-2)$$

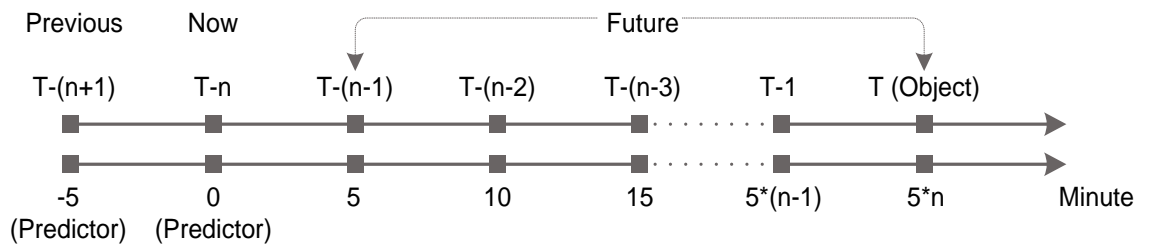
For example, if we want to predict half an hour in advance, namely HT equals 30 minutes, then 'n' is 6. As the time horizon is up to 3 hours ahead, the maximum n is 36. The figures below show how the time step corresponds to different forecast horizon times.



(a) - Horizon time = 5 minutes



(b) - Horizon time = 15 minutes



(c) - Horizon time = 5*n minutes

Figure 2-2 Examples of horizon time

Using an AR(2) model implies that the predictors are taken at -5 and 0 minutes. These two predictors are then related to different 'n's depending on the horizon time considered.

Forecast produced at time T uses values from the two previous time steps, T-n and T-(n+1). Given our use of 5-minute averaged data, T-n and T-(n+1) correspond to the previous 5 n- and 5 (n+1)-minute averages respectively. The coefficients, α , β_1 , β_2 , γ_1 , γ_2 , δ_1 and δ_2 are parameters to be fitted by the multi-linear regression method.

2.1.2.2 Random Forest model

Based on training data set, machine learning is basically an application of artificial intelligence (AI) which has the ability to learn and do data mining without being explicitly programmed. It can also provide an effective way for discovering and extracting regularities among different data. Without involving human participation, the process of acquisition of knowledge from experience is much less time-consuming and it is, with no doubt, a symbol of high level automation [19]. Some popular machine learning algorithms such as Artificial Neural Network (ANN) and Support Vector Machine (SVM) are now widely used in data mining, images analysis and so on. Random Forest, as one of the powerful machine learning tools, is introduced and used in this research.

Random Forest (RF) is a widely used statistical machine learning method developed by Breiman [4] and Cutler et al. [5]. It constructs multiple-predictor models and can be used for both regression and classification problems. For regression, as it is used here, its algorithm contains three major steps [22]. First, N bootstrap samples are drawn with each sample including approximately 64% of the original training data. A basic structure of

the original training data is shown in equation (2-3). In this training data set there are 6 features, from A to F, and m samples, from 1 to m .

$$T = \begin{bmatrix} X_{A1} & X_{B1} & \cdots & X_{F1} & Y_1 \\ X_{A2} & X_{B2} & & X_{F2} & Y_2 \\ \vdots & & & \ddots & \vdots \\ X_{A12} & X_{B12} & & X_{F12} & Y_{12} \\ \vdots & & & \vdots & \vdots \\ X_{Am} & X_{Bm} & \cdots & X_{Fm} & Y_m \end{bmatrix} \quad (2-3)$$

where x denotes the feature and y is the object (solar irradiance or power output, in our case). Then, an unpruned regression tree is grown for each of the bootstrap samples. However, rather than using the best split among all p predictors, only m of the p predictors are randomly sampled and the best split is chosen from among these m variables.

$$S = \begin{bmatrix} X_{A3} & X_{B3} & \cdots & X_{F3} & Y_3 \\ \vdots & & & \ddots & \vdots \\ X_{A12} & X_{B12} & \cdots & X_{F12} & Y_{12} \end{bmatrix} \quad (2-4)$$

Note that S is a subset of the training data set T and each subset is used to develop a specific decision tree. Finally, the prediction is formed by averaging the output of the N trees (or equations). In addition to constructing multiple-predictor models, RF also produces scores measuring the relative importance of each predictor on the predictand. This score is estimated by calculating the mean decrease in accuracy due to permuting the associated predictor while leaving the others unchanged [22].

$$Y_p = \frac{1}{N} \sum_{n=1}^N T_n(X) \quad (2-5)$$

where Y_p is the predictand, T_n denotes the decision tree function, and X is a vector with different features. In practice, the advantages of the RF method include:

- Relatively high speed of learning

- Robustness (effectively avoid over-fitting)
- Variable importance of predictors is provided
- Missing data can be estimated

2.1.2.3 Persistence

Persistence is conceptually the simplest prediction model. In its simplest form, it consists in keeping constant (persisting) the last measured value, therefore assuming that the value at the current time of the quantity to be predicted is the same as its value at the previous time step. For instance, if the temperature yesterday were 20° C, the simplest persistence forecast would predict 20° C also for today. Formally this is expressed as:

$$P(t_2) = P(t_1) \quad (2-6)$$

where t_2 is the current time step and t_1 is a previous time step.

More elaborated forms of persistence could be formulated, whereby also values at previous time steps (as for autoregressive methods) or physical features may be considered. In our case, since solar irradiance typically has a pronounced diurnal cycle, and because the solar cycle – the irradiance under clear sky conditions – can be easily computed well in advance, a slightly modified version of persistence is more appropriate. Hence, instead of persisting the full signal of irradiance, the difference between irradiance and the clear sky value is persisted. Thus in the case of GHI:

$$GHI(t_2) = GHI(t_1) + (CS(t_2) - CS(t_1)) = (GHI(t_1) - CS(t_1)) + CS(t_2) \quad (2-7)$$

where CS is the irradiance under clear sky conditions. We will refer to this modified persistence for GHI as *gap persistence*. It is worth noticing that a fixed turbidity is used

for figuring out the clear sky irradiance in Canberra region. In principle, this could be varied, especially considering the seasonality of the index, but since we are considering seasons separately this effect would not be very pronounced. Also, the turbidity is largely dependent on aerosol loading. In order to get precise turbidity, aerosols measurements are required. However, these are normally not readily available and incur extra measuring equipment costs. Canberra, however, has a relatively low aerosol loading and variability, which means that the turbidity would not fluctuate tremendously. All the factors described above contribute to the reason why a fixed turbidity rather than a varied one is used in this study.

The persistence method is a simple approach and the performance in short time-frame prediction such as intra-minute solar energy forecast is reliable. For overcast or sunshine days, the steady-change weather conditions will also contribute to the forecast quality of persistence model, which will make it difficult to improve upon accuracy. One major limitation of persistence, however, is that it heavily relies on local observations, more so than other statistical approaches such as those described above, which can benefit from other relationships inherent to longer historical data. Besides, the persistence method may not do well under partly cloudy sky conditions and in a long lead-time context.

2.1.3 Prediction set up and Assessment

Predictions are performed at various lead times from five minutes (the granularity of the data) to 3 hours. Given the pronounced seasonal dependence of solar irradiance, predictions are performed separately for both winter and summer. A three-month period is used for the training of the statistical methods. The prediction is then tested over the ensuing month. Thus, for summer, the training period is from 1 November 2012 to 31 January

2013 and the prediction period is from 1 to 28 February 2013. For winter, the training period is from 1 May to 31 July 2012 and the prediction period is from 1 to 31 August 2012.

Figure 2-3 shows the clear-sky index (a standard proxy for sky conditions) distribution for the Namadgi School site for summer (top panel) and winter (bottom panel). The seasonality of the sky condition is apparent: winter is dominated by clear sky conditions – around 60% of events have a clear-sky index higher than 0.9 – while in summer, there is a predominance of clear-sky index values in the three ranges, 0.2-0.5 (cloudy conditions, ca. 25%), 0.8-0.9 (broken cloud conditions, ca. 20%) and higher than 0.9 (clear, ca. 30%). It is worth to note that for both seasons the distribution of the clear-sky index is roughly the same in both the training and prediction periods.

The success of the three prediction methods – multi-linear, random forest and gap persistence – is assessed by means of the relative mean absolute error (rMAE). The other two common metrics, correlation coefficient and relative root-mean-square error, were also assessed alongside the rMAE but since they showed the same features as rMAE only the latter was retained for simplicity of presentation. The denominator used to compute the rMAE is the mean GHI measurement value over the prediction period.

Also, we only assess daytime values of GHI and power output. Night time, as well as early morning and early evening values are masked. For the latter two, the masking is imposed at times for which the clear sky irradiance is less than 50 W m^{-2} .

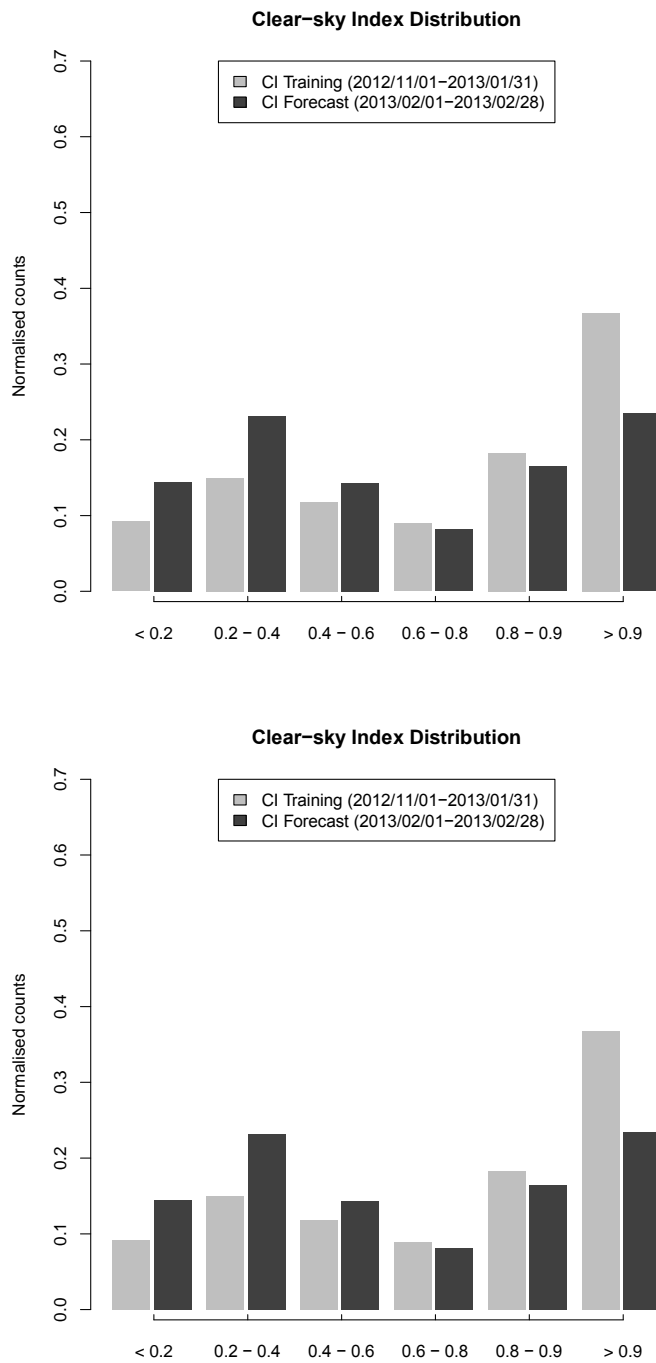


Figure 2-3 Clear-sky index Distribution at Namadgi School for summer (top) and winter (bottom) and for both training period (grey bars) and prediction period (black bars).

2.2 Relative importance of predictors

In this section we assess the relative importance of a number of meteorological predictors for the prediction of solar irradiance at the Namadgi School site. We then include PV

system related predictors for the power predictions. We test most of the variables measured at the monitoring stations, including solar irradiance, temperature, humidity, pressure, wind speed and precipitation. In this study, up to three variables at a time along with the extra-terrestrial solar irradiance are tested. A preliminary assessment of the importance of predictors is also carried out by computing the linear correlation coefficients between the predictand (GHI or solar power output) and the predictors.

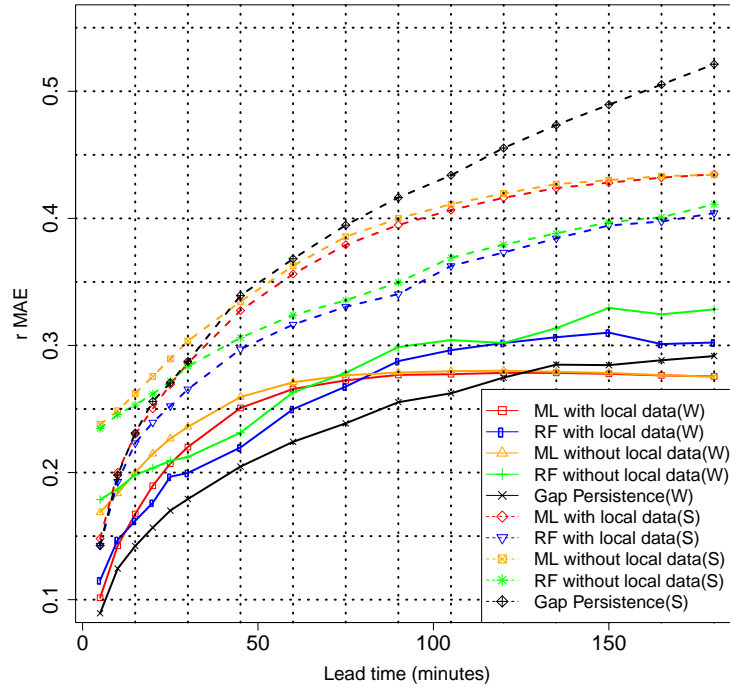
Different meteorological variables contribute differently to prediction results. PV power output mainly depends on solar irradiance and solar panel temperature. In turn GHI depends on the sun position, cloud cover, humidity etc. Also, solar panel temperature can be influenced by solar irradiance and air temperature. Wind speed can affect both GHI, insofar as it relates to cloud speed, and PV power output, through heat transfer via local air advection. However, note that our wind measurements, taken at the rooftop level, are representative of the local PV panel environment and are not in general representative of higher level atmospheric flow; for the purpose of cloud movement, atmospheric pressure (or its temporal variations) could be a better indicator. Humidity levels provide a proxy for the amount of direct irradiance absorption. In addition, the extra-terrestrial solar irradiance, which can easily be computed (e.g. using the R package ‘RAtmosphere’), is selected as a fixed predictor in all predictions. Extra-terrestrial solar irradiance embeds the local time and seasonality of the GHI.

Figure 2-4 shows the rMAE of GHI prediction in summer (dashed lines) and winter (solid lines) for four sets of predictor combinations. Before delving into the relative importance of variables it is interesting to note a few general features. Firstly, prediction skill is higher in winter (lower rMAEs) than in summer. The seasonality in skill is not surprising given the marked difference in sky conditions in the two seasons (Figure 2-3), as we will also

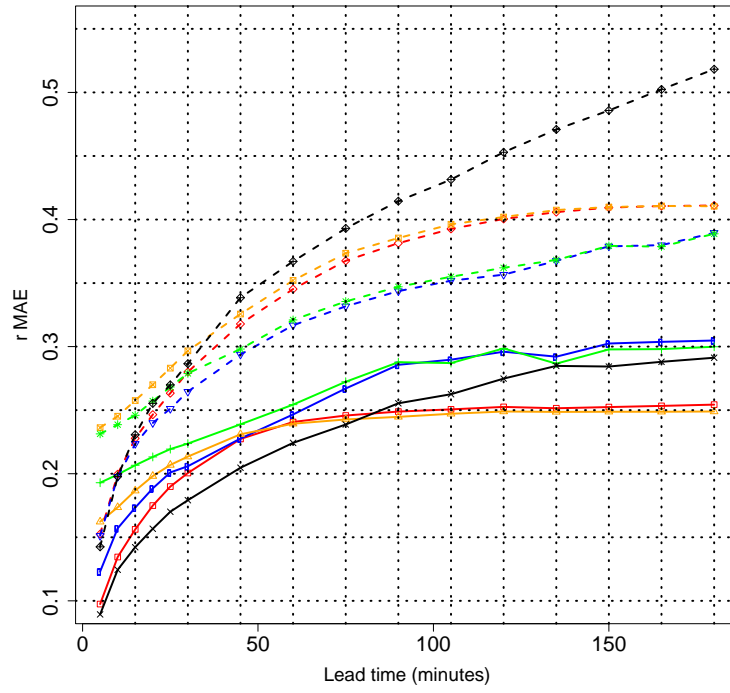
see in section 2.4.1. Specifically, the summer rMAE ranges from 0.15 to 0.53 while in winter it ranges from 0.09 to 0.34. Secondly, for corresponding statistical methods, when local data (i.e., from the Namadgi School station) are used the forecast accuracy is noticeably higher for lead times up to about 45 minutes. However, for longer lead times, the difference between prediction with and without local data is normally negligible. Thirdly, gap persistence provides a better prediction than that without local data up to about 15 minutes in summer. For longer lead times gap persistence rapidly degrades, reaching values larger than 0.5 for lead times close to 3 hours. In winter, however, gap persistence is often more accurate than the predictions without local data, for lead times up to around 90 minutes (Figure 2-4 (b)-(d)) and even 120 minutes as in the case of Figure 2-4 (a). Surprisingly, gap persistence outperforms even predictions with local data (for the same mentioned lead times). Fourthly, when the two statistical methods are compared, it is apparent that Random Forest is better than the multi-linear method in summer. The opposite is normally true in winter, however.

In terms of relative importance of predictors, the difference in accuracy amongst the four cases is not large. Nonetheless, in summer the best GHI prediction is obtained when GHI, air temperature and absolute humidity are taken as predictors (Figure 2-4 (c)). In winter the best set of predictors is with GHI, pressure and absolute humidity (Figure 2-4 (b)). Table 2-1 summarises the best predictor (and method) options for GHI predictions. Note that since all the cases include the extra-terrestrial solar irradiance as a predictor, this is not listed in the table.

(a)



(b)



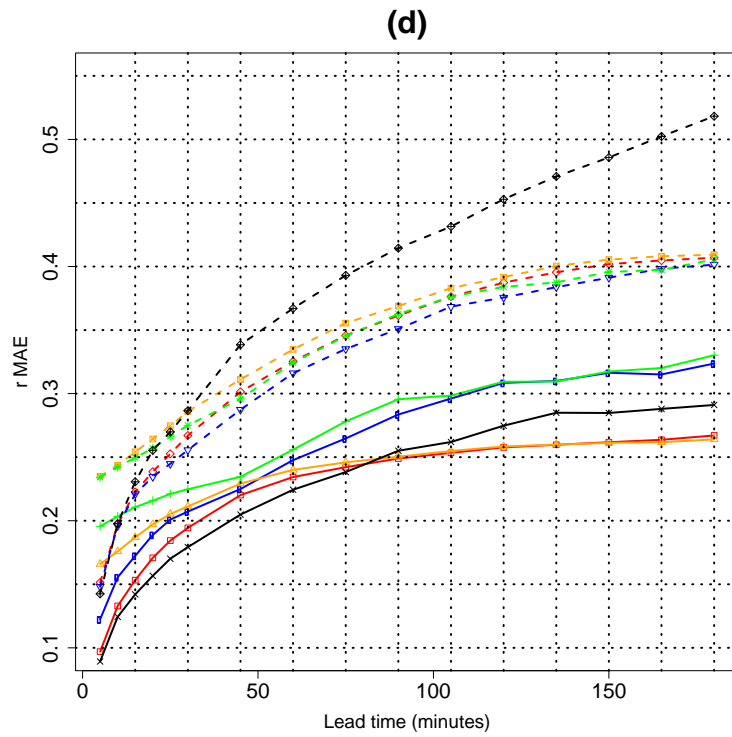
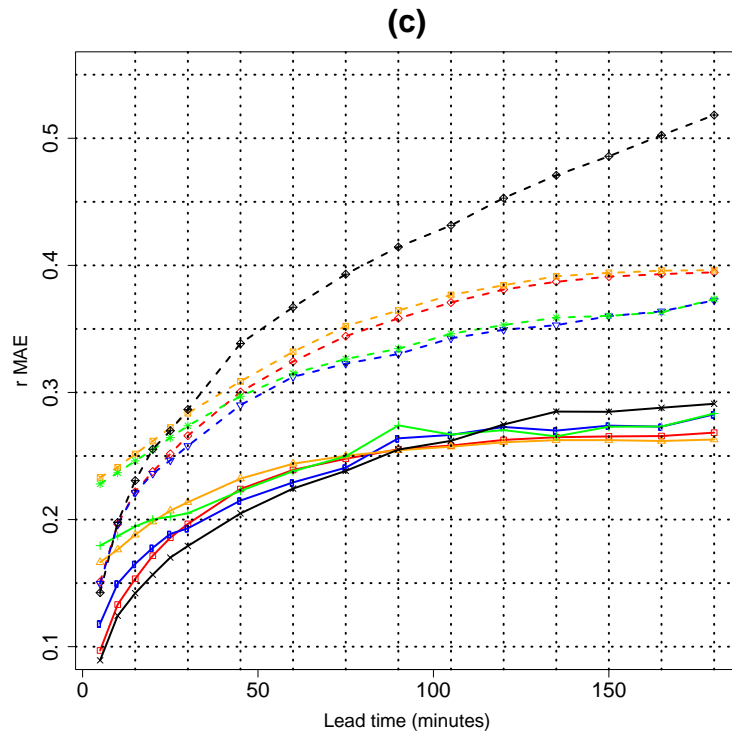


Figure 2-4 rMAE of GHI Prediction. (a) Predictors: GHI only; (b) Predictors: GHI, Air Pressure, Absolute Humidity; (c) Predictors: GHI, Air Temperature, Absolute Humidity; (d) Predictors: GHI, Air Temperature, Air Pressure (Dashed lines show results for summer, solid lines for winter).

		Summer		Winter	
		Method	Predictors	Method	Predictors
Short lead-time	With local data	Random Forest	GHI, Air Temperature, Humidity	Clear Sky Persistence	GHI
	W/o local data	Random Forest	GHI, Air Temperature, Humidity	Multi-linear	GHI, Pressure, Humidity
Longer lead-time	With local data	Random Forest	GHI, Air Temperature, Humidity	Multi-linear	GHI, Pressure, Humidity
	W/o local data	Random Forest	GHI, Air Temperature, Humidity	Multi-linear	GHI, Pressure, Humidity

Table 2-1 Best options for GHI prediction

Figure 2-5 shows the analogous rMAE values as discussed for power prediction. Here, the observed solar irradiance on PV plane (SP-Solar) is also selected as one of the predictors (Figure 2-5 (a)). Other predictor combinations have been tested but only these two are shown for brevity. Similar considerations to those for the case of GHI prediction apply here, with a few exceptions. When using SP-Solar as a predictor, there is a decrease in rMAE (equivalent to an increase in accuracy) for lead times from 5 minute to just over an hour. While this increase in skill may be surprising at first glance, it can be explained by the fact that the three PV systems have different tilt and orientation angles. Incidentally, this is basically equivalent to using the raw PV output from neighbouring devices (e.g. from pvoutput.org): even for geographically close PV systems, these can have markedly

different output behaviour due to roof configurations, possible shading by trees, and other considerations.

Although noticeable even when GHI, instead of SP-Solar, is used as a predictor, this effect is much reduced (Figure 2-5 (b)). While the forecast accuracy is lower with local GHI observations compared to when local SP-Solar is used, particularly at lead times below about 60 minutes, predictions without local data are more accurate when GHI turns out to be a better predictor than SP-Solar, as tilted solar irradiance is more site-specific.

In terms of predictors, SP-Solar, solar panel temperature and absolute humidity (Figure 2-5 (a)) seem to provide the most accurate prediction in both summer and winter, especially when local data is used. The best options for PV power predictions are listed in Table 2-2.

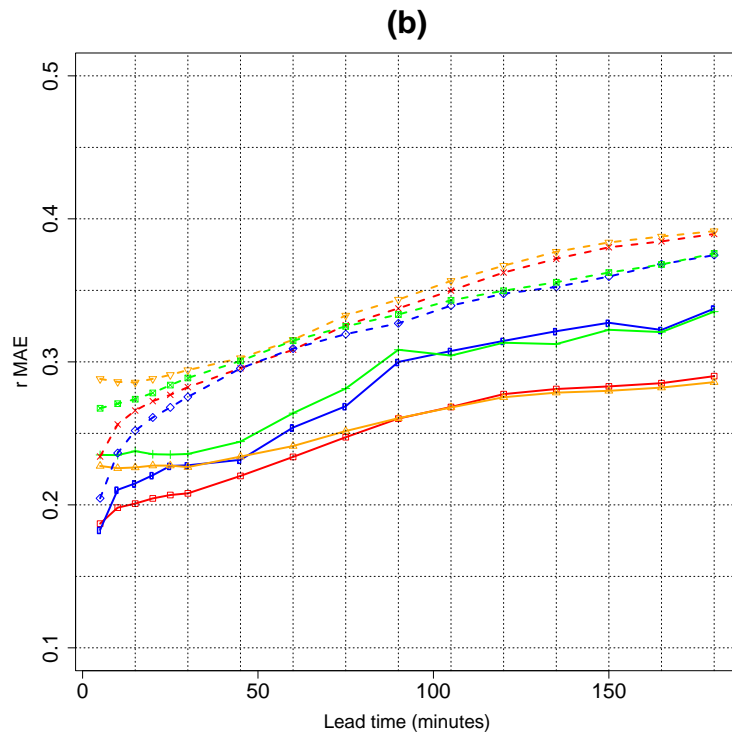
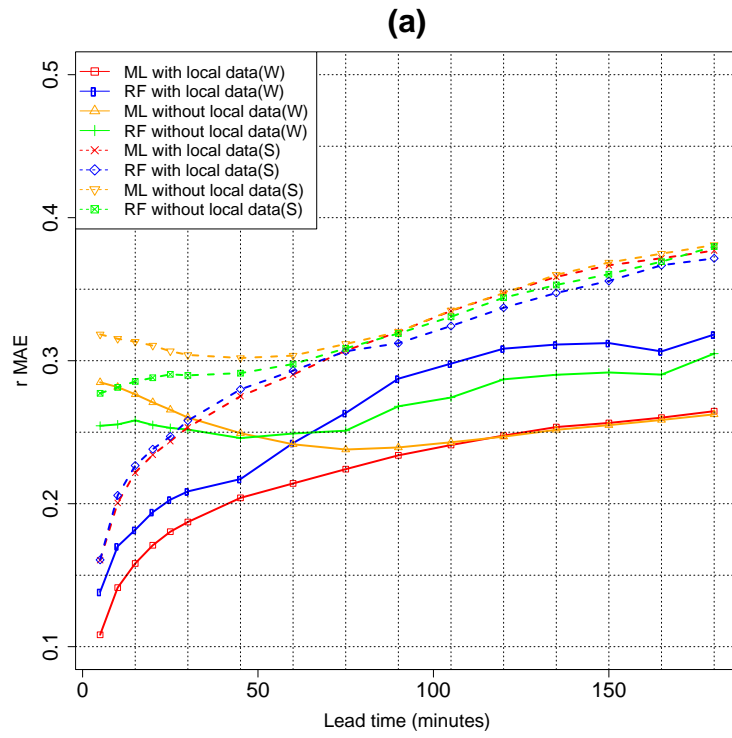


Figure 2-5 rMAE of Power Prediction. (a) Predictors: Global Irradiance on Tilted Surface (SP-Solar), PV panel temperature, Absolute Humidity; (b) Predictors: GHI, Air Temperature, Absolute Humidity. Dashed lines show results for summer, solid lines for winter.

		Summer		Winter	
		Method	Predictors	Method	Predictors
Short lead-time	With local data	Multi-linear	Tilted Global Irradiance; Panels Temperature; Humidity	Random Forest	Tilted Global Irradiance; Panels Temperature; Humidity
	W/o local data	Random Forest	GHI, Air Temperature, Humidity	Random Forest	GHI, Air Temperature, Humidity
Longer lead-time	With local data	Random Forest	Tilted Global Irradiance; Panels Temperature; Humidity	Multi-linear	Tilted Global Irradiance; Panels Temperature; Humidity
	W/o local data	Random Forest	Tilted Global Irradiance; Panels Temperature; Humidity	Multi-linear	Tilted Global Irradiance; Panels Temperature; Humidity

Table 2-2 Best options for power prediction.

2.3 Relative importance of monitoring stations

In order to assess the relative importance of each of the monitoring stations, observations from the Black Mountain and Wombat Hill stations are used both in combinations and separately to predict GHI at the Namadgi School station. As seen in the previous section, if local data are available, the performance of GHI and PV power output forecasts is expectedly better, particularly when the lead time is short.

Figure 2-6 shows the rMAEs for the GHI prediction using different combinations of the three sites Black Mountain, Wombat Hill and Namadgi School and applying the random forest method for summer and the multi-linear method in winter. The red line shows the rMAE when all three stations are used, whereas the blue line represents the two non-target stations, Black Mountain and Wombat Hill. A combination of target and non-target stations is given by the yellow line (Wombat Hill and Namadgi School) and purple line (Black Mountain and Namadgi School). The green and brown lines are for just Wombat Hill and Black Mountain, respectively. Finally, the black line represents gap persistence.

Figure 2-6 (a) shows the rMAE of GHI prediction in summer. It can be seen that when the observations from the target site, Namadgi School, are included (red, yellow and purple lines) prediction results expectedly outperform those of the other three cases for short lead times (up to about 30 minutes), with the red line (all three stations at once) providing the best prediction (over all lead times). For longer lead times, however, using only the two non-target stations, Black Mountain and Wombat Hill (blue line), yields comparable results to having the target site included. It is also apparent that the combined use of Black Mountain and Wombat Hill is superior to the case when only one of the two is used (brown line in the case of Black Mountain or green line for Wombat Hill). However, Wombat Hill alone performs considerably better than Black Mountain to lead times of about 100 minutes, whereas the situation is reversed for longer lead times (to 3 hours).

The analogous case for winter is presented in Figure 2-6 (b). As in the previous section, we can see again here the overall higher forecasting quality in winter than in summer. Not only is the accuracy higher in winter from the outset (5-minute lead time), the rate of rMAE increase is also considerably lower in winter than in summer. Similar to summer, the prediction performance is higher when local data are used, for lead times less than 45

minutes. As the lead time increases, the role of the local data clearly reduces. The role of the Black Mountain data (brown line) is particularly noticeable for lead times beyond 90 minutes: using this station alone the forecast skill is superior than with any other combination of data. As already observed in Figure 2-4, the most evident feature is the accuracy of gap persistence: this can predict GHI better than the two more sophisticated statistical models for short lead times. This is again a reflection of the predominant clear sky conditions, which characterize Canberra in winter.

Based on the above results, some conclusions can be drawn. The main reason why, in most cases, Black Mountain yields more accurate predictions than Wombat Hill is that meteorological conditions at Namadgi School are similar, and often lag, those at Black Mountain. However, in summer a pronounced occurrence of south-easterlies, due to the effect of sea breezes, means that predictors from Wombat Hill are more important than those at Black Mountain. This is particularly the case for February 2013, the test period for the summer case (not shown). As a consequence, predictors from Wombat Hill outperform those from Black Mountain in summer. An additional factor in the forecasting performance may be related to the stations' elevation. Specifically, while Black Mountain is at about the same elevation as Namadgi School, Wombat Hill is ca. 350 m higher.

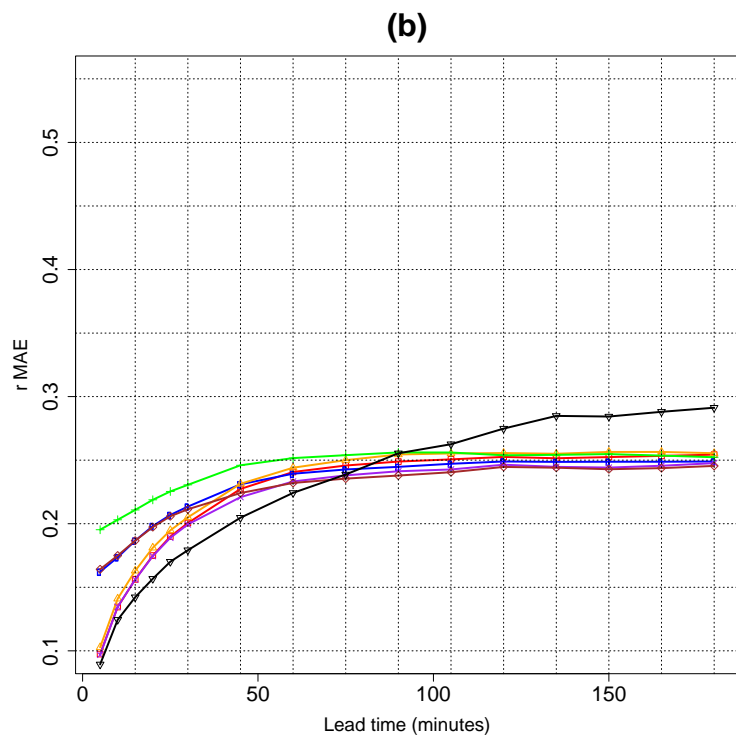
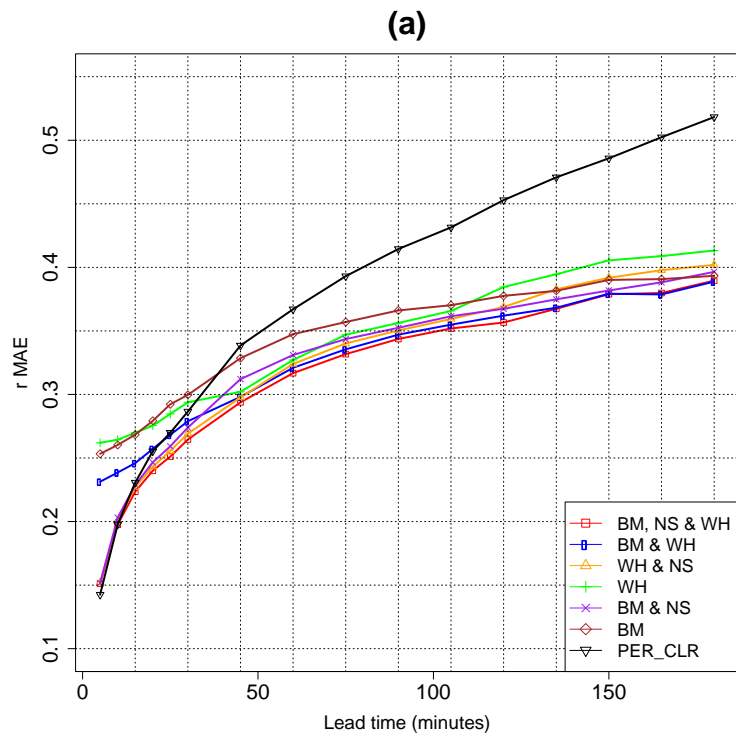


Figure 2-6 rMAE of GHI predictions using data from different stations (a) in summer (Method: Random Forest; Predictors: GHI, Air Pressure, Absolute Humidity); (b) in winter (Method: Multi-Linear; Predictors: GHI, Air Pressure, Absolute Humidity).

2.4 Conversion of GHI prediction into power prediction

As noted above (e.g. Figure 2-5), unlike the GHI, prediction of PV power output is strongly site-specific. Specifically, when local data are not used, direct use of global irradiance on PV planes from neighbouring systems (a site-specific variable) is expectedly a worse predictor than using GHI (a general variable), as demonstrated by the marked decreases in rMAE over lead times up to about 60 minutes (Figure 2-5 (a)). This abnormal increase in accuracy with lead time is related to the (different) geometry of the PV systems considered. Thus, correcting for the site-specific nature of the predictor should improve the prediction quality.

We explore an empirical approach to predicting PV power for situations when the only available information about the target PV system is its tilt and orientation angle. Table 2-1 shows the tilt and orientation angles of the three stations used in this research. The approach also assumes the knowledge of the relationship between the three components of solar irradiance, which are necessary to derive global irradiance on a generic plane (namely, other than horizontal). Measurements of either DNI or diffuse irradiance (or both) are therefore required. Although these measurements are less common than GHI, they are available at a number of sites. Besides, given that the statistical relationships between the three irradiance components hold over a wide spatial extent, say within tens of kilometres (this distance depends on the local orography and climatology of the area), such measurements do not necessarily need to be taken at the target site. In our case, the three components are measured only at the Black Mountain site. We then assume that their relationships hold for the other two sites, Namadgi School and Wombat Hill.

Station	Tilt Angle (°)	Orientation Angle (°)
Black Mountain	36	38 (Facing Northeast)
Namadgi School	25	327 (Facing Northwest)
Wombat Hill	21	31 (Facing Northeast)

Table 2-3 Tilt and orientation angles of the three PV systems.

Essentially this approach involves an empirical geometry conversion, which transforms global horizontal irradiance into global irradiance on a tilt surface (a surface with the same tilt angle and orientation angle as the target station). It also requires historical observations for at least two radiation components in order to compute the relationship between the Diffuse Fraction (DF, which is the ratio between Diff and GHI) and the clear-sky index [3]. Here, data for the three radiation components from the Black Mountain site have been used to build such relationship (Figure 2-7).

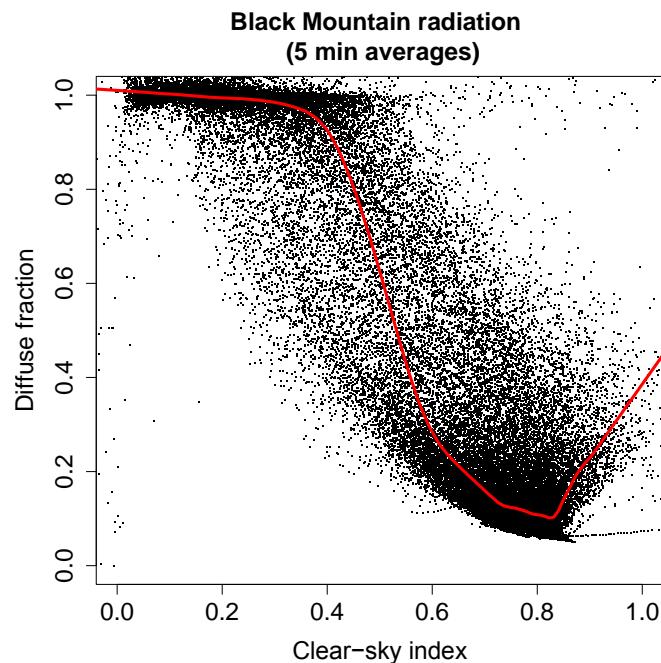


Figure 2-7 Diffuse Fraction versus clear-sky index for Black Mountain station. The red line is the fitted line using the loess R function.

Assuming the same relationship applies to nearby locations, the diffuse and the DNI at the target station can be estimated using just the GHI at the target station. Then, the global

irradiance on a tilted plane can be approximated as the sum of the direct irradiance on the plane, which can be expressed as a geometrical transformation of DNI, and the (modified) diffuse component. Thus, the steps of this conversion are as follows:

1. Fit an empirical curve to the relationship between diffuse fraction and the clear-sky index at a nearby location. Figure 2-7 shows the fitted line, computed with the *R loess* function, for Black Mountain.
2. For a given clear-sky index (and hence GHI) derive the corresponding DF by using the fitted curve. The horizontal diffuse component is then estimated by using the relationship:

$$\text{Diff}_{\text{Est}_h} = \text{GHI} * \text{DF} \quad (2-8)$$

where $\text{Diff}_{\text{Est}_h}$ is the estimated horizontal diffuse component.

3. Estimate DNI, via the relationship $\text{GHI} = \text{DNI} \cos \theta_z + \text{Diff}$:

$$\text{DNI}_{\text{Est}} = \frac{\text{GHI} - \text{Diff}_{\text{Est}_h}}{\cos \theta_z} \quad (2-9)$$

where DNI_{Est} is the DNI estimation, and θ_z is the solar zenith angle.

4. Compute the angle of solar incidence by using the tilt angle and orientation angle of the target station (Namadgi School) as follows:

$$\cos \theta = \cos \theta_z * \cos \beta + \sin \theta_z * \sin \beta * \cos(\gamma_s - \gamma) \quad (2-10)$$

where θ is the angle of incidence, β is the tilt angle, γ_s is the solar azimuth angle and γ is the azimuth angle of a tilted surface.

5. Compute the direct irradiance on a tilted surface:

$$DI_{\text{Tilted_Est}} = DNI_{\text{Est}} * \cos \theta \quad (2-11)$$

where $DI_{\text{Tilted_Est}}$ is the direct irradiance on a tilted surface.

6. Compute the global irradiance on a tilted surface by combining the direct irradiance and diffuse component, by assuming that the ground reflection is negligible and the diffuse component, $\text{Diff}_{\text{Est_h}}$, is isotropic [27]:

$$GI_{\text{Tilted_Est}} = DI_{\text{Tilted_Est}} + \frac{(1 + \cos \beta)}{2} \text{Diff}_{\text{Est_h}} \quad (2-12)$$

By following the steps listed above, a virtual PV system – using the tilt and orientation angles of the target station – can be set up for different locations, whereby the corresponding global irradiance on the target tilted surface can be computed [3].

Once the solar irradiance on plane of non-local stations is reconstructed as shown above, it can be used as the key predictor for PV power output prediction. In fact, even though three predictors are chosen in every single prediction, the new solar irradiance on a tilted surface with the same angles (both the tilt and orientation) of the target station is the most important predictor.

Taking Table 2-2 as a reference, the other two predictors are PV panel temperature and absolute humidity. Absolute humidity is taken directly from historical data. However, since PV panel temperature is not a variable commonly available and in order to make the prediction algorithm as applicable as possible to generic target stations, the PV panel temperature is derived using the following relationship:

$$T_{\text{sp}} = T_a + \alpha_1 * GHI + \alpha_2 \quad (2-13)$$

where T_{sp} is the solar panel temperature, T_a is the ambient air temperature of the target station, GHI is measured at different stations, and α_1 and α_2 are two coefficients computed from historical data.

Thus, PV power output at the target station is computed by means of the multi-linear and Random Forest methods, and using the three predictors: derived solar irradiance on a plane, estimated panel temperature and absolute humidity. The multi-linear method is applied as the main forecast algorithm in winter, as it is superior to Random Forest in this season (Table 2-2), while Random Forest is used in summer.

Figure 2-8 shows the forecast results of the PV power prediction. When local data are not used/available, the approach presented in this section provides an improvement with respect to using GHI (Figure 2-5 (b)) at short lead times (under 30 minutes). This is valid for both winter and summer – compare orange solid and green dashed lines in Figure 2-5 (b) (which shows the best forecast quality between the two panels for short lead times and without local data) with the corresponding blue lines in Figure 2-8 (a)-(b). For longer lead times, the performance of the prediction deteriorates a little faster than the counterpart in Figure 2-5. While the predictions shown in Figure 2-5 use predictors taken directly from historical data, for predictions in Figure 2-8, the global irradiance on tilted surface and the solar panels temperature are both reconstructed based on GHI measurement. The dependency of these two variables, and the fact that there are approximations in the algorithm presented in this section, may be the reason for such deterioration.

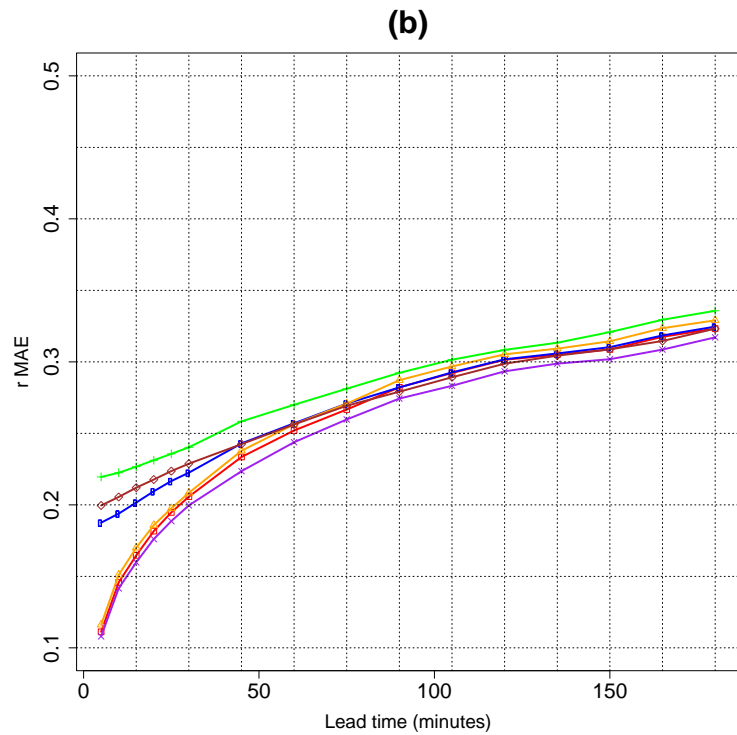
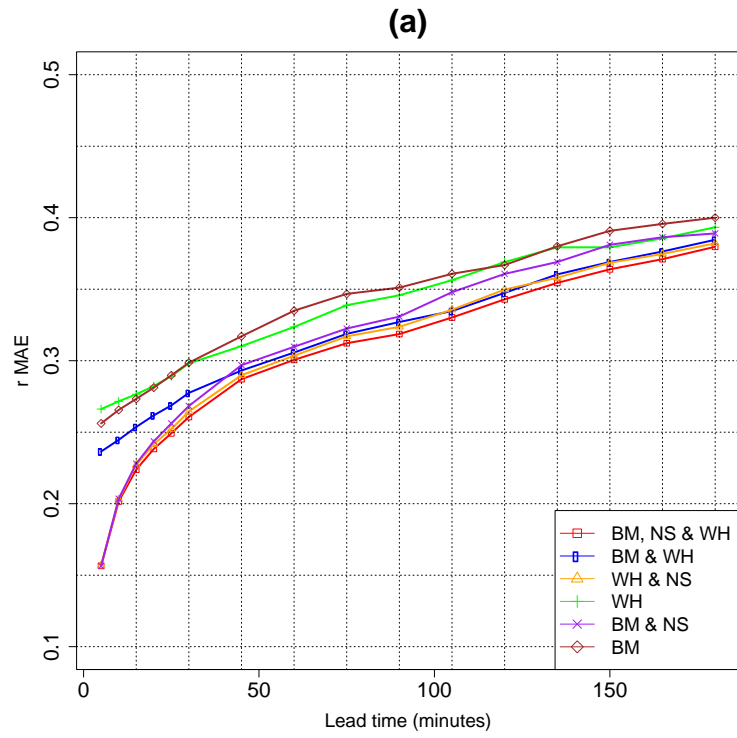


Figure 2-8 $rMAE$ of modified Power predictions based on the conversion presented in Section 5 and using data from different stations (a) in summer (Method: Random Forest; Predictors: SP-Solar, PV panel temperature, Absolute Humidity); (b) in winter (Method: Multi-Linear; Predictors: SP-Solar, PV panel temperature, Absolute Humidity).

2.4.1 Dependency of power prediction on sky conditions

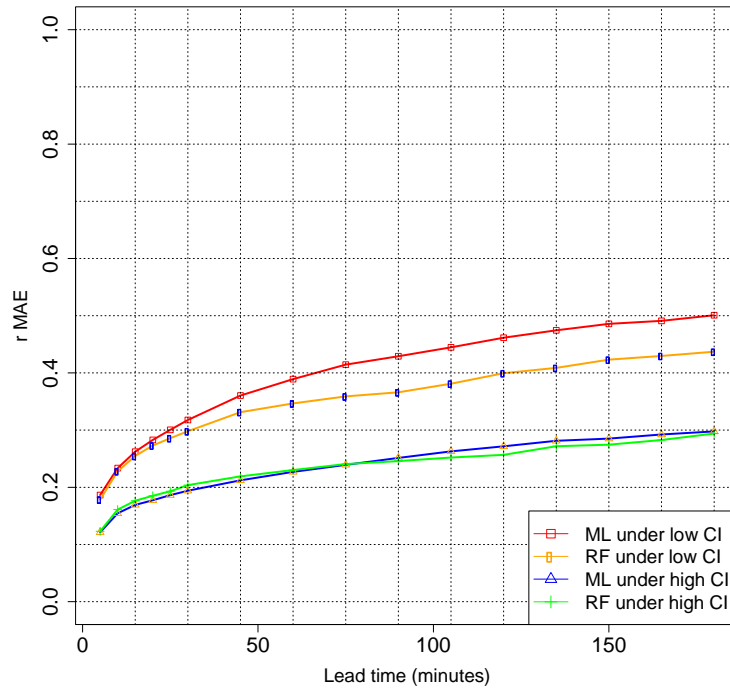
Performance of solar predictions depends on the sky conditions, with predictions under clear skies normally considerably more skilful than under variable cloud conditions. We already observed this effect when we compared the forecast skills for winter and summer (Figure 2-4, Figure 2-5, Figure 2-6 and Figure 2-8).

In this section we assess the dependency of forecast skill on sky conditions within each season and also across statistical models. Figure 2-9 shows the rMAE of power output prediction (when the geometry transformation described in the previous section is used) under two types of sky conditions, namely clear sky (high clear-sky index) and variable/overcast conditions (lower clear-sky index). We define as clear sky conditions events for which the clear-sky index is higher than 0.9. While in winter the gap in prediction skill between clear and non-clear sky conditions is obvious at all lead times, with rMAE differences by up to 0.7 in favour of clear sky conditions (Figure 2-9 (c)-(d)), in summer the performance gap between different sky conditions is not as large as that in winter. This is partly due to the fact that many events (almost 20%) fall in the category next to the chosen threshold of 0.9, namely in the 0.8-0.9 category (Figure 2-3). Specifically, some of these events could be practically considered as clear sky conditions for the summer period. This is because the amount of diffuse fraction under clear sky conditions is normally higher in summer, due to higher water vapour and aerosol levels, which therefore leads to a reduction of the clear-sky index even if the sky is cloudless.

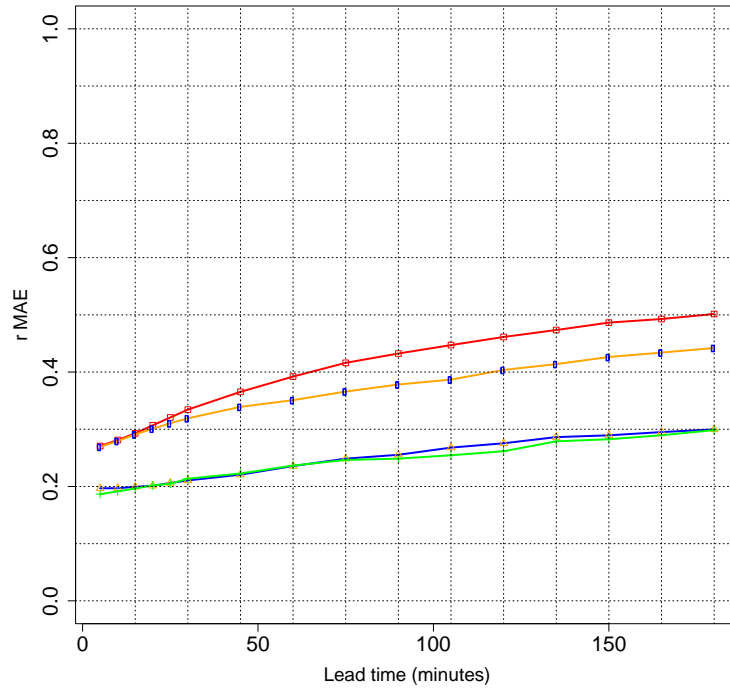
Figure 2-9 also provides a comparison of the skill of the two statistical methods, the multi-linear and the random forest. Aside from the case of clear sky conditions in winter, when

the multi linear method is superior to random forest, in all other cases random forest provides more skilful forecasts. This is not very surprising since solar radiation is highly non-linear –except in cases when clear sky conditions are predominant as in the winter case here. At the same time it is encouraging to note that the random forest method is able to capture such non-linearity better than a linear approach does.

(a)



(b)



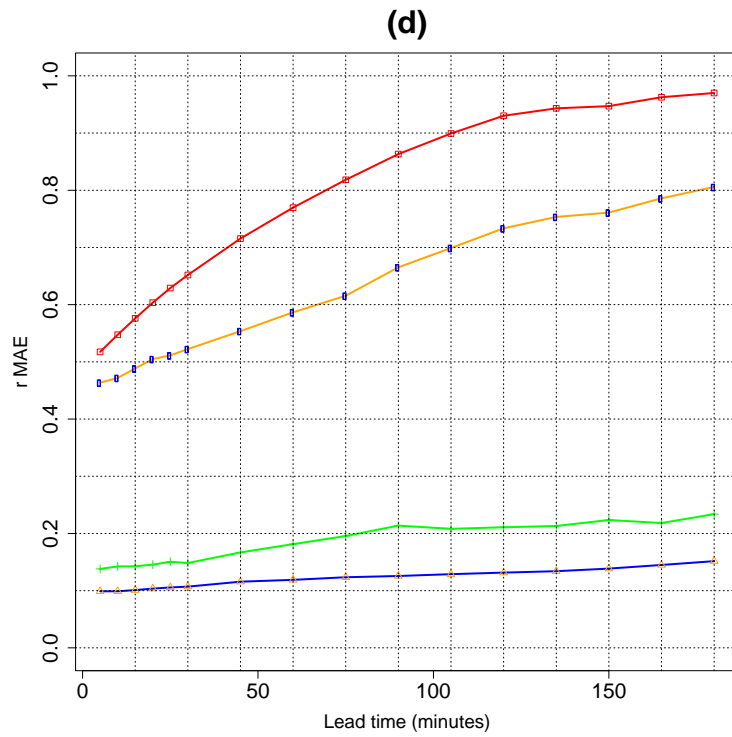
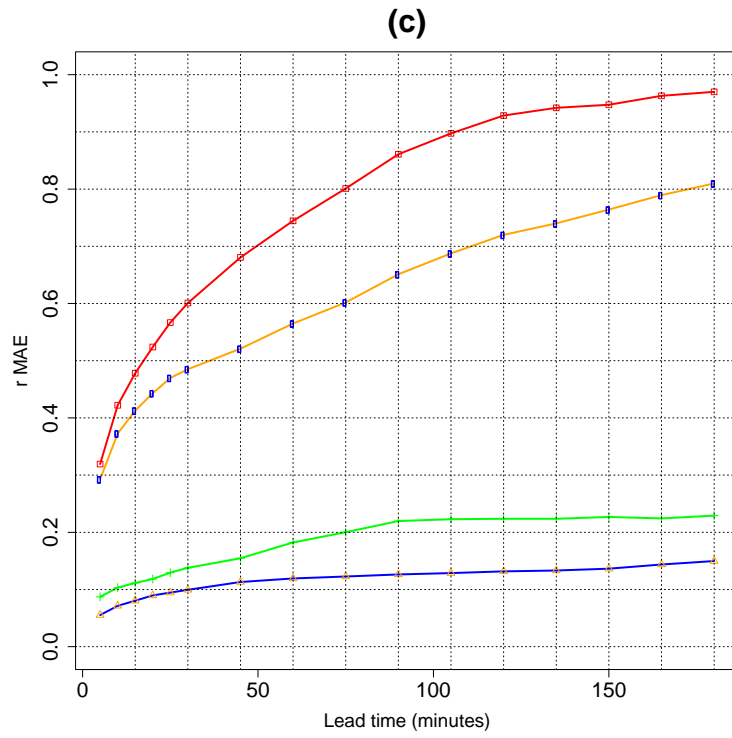


Figure 2-9 rMAE of Power prediction under clear sky and non-clear sky conditions (station used: Black Mountain and Wombat Hill; Predictors: SP-Solar, PV panel temperature, Absolute Humidity). (a) Summer, with local data; (b) Summer, without local data; (c) Winter, with local data; (d) Winter, without local data

Chapter 3 Test Platform and Control for the Integrated PV Solar and Battery System

3.1 Test System

After prediction on solar irradiance/power is derived, the problem of how to use it in a solar-based system remains to be solved. Therefore, in this chapter, a test system is proposed where the prediction of solar irradiance/power is applied to work out the reference trajectory of the battery terminal voltage.

The solar panels, battery and converters will be used to test the performance of the short term solar radiance prediction algorithms to provide a constant power to the load. The solar output has a variability which can be compensated by the battery. In this system, the objective will be to set up a 100 percent renewable energy stand-alone system without purchasing power from the grid and balance the power generation and consumption under a variety of constraints. This simulation will enable research in how solar irradiance prediction can be used in a physical model and how the prediction quality influences the overall outcomes.

According to the objective identified above, the system is isolated which means that there is no link between this system and the grid, and the main physical components include PV cells, battery, DC converters and the load. Besides, there is a DC bus for linking all the components together. As the power from the PV panels goes towards one direction only which is generally from solar panels to DC bus, the DC-DC converter linked between them is a unidirectional one. However, the power can flow in or out of the battery banks.

Therefore, the converter used between the battery and DC bus is bidirectional. In order to gain a proper voltage of the DC bus as well as to realize power balance under a variety of limits (such as battery charging or discharging rate or SOC constraints of the battery), two different controllers are used with the unidirectional converter and the bidirectional converter. The electric circuit is shown in Figure 3-1. S1, S2 are the control signals for the bidirectional converter while S3 is the control signal for the PV side converter.

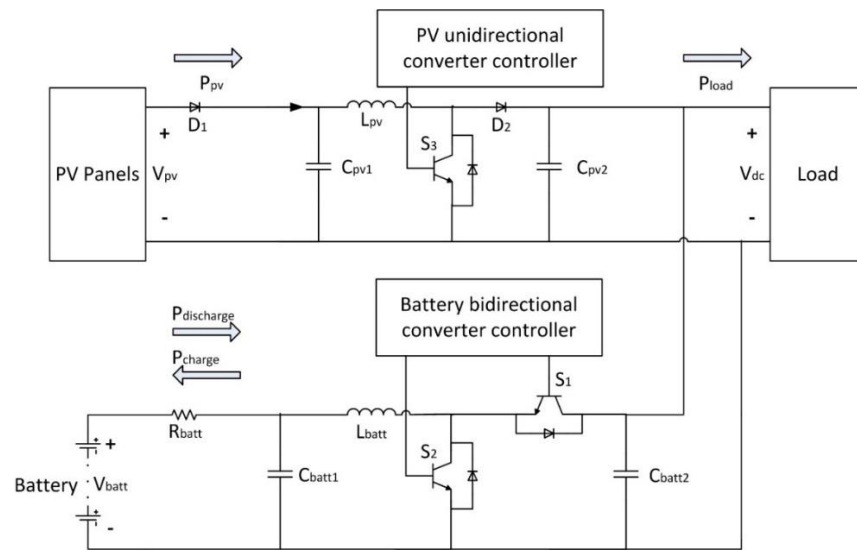


Figure 3-1 System topology of the PV-Battery hybrid system (R: resistance; L: inductance; C: capacitance)

3.2 System Modelling

3.2.1 Modelling of the unidirectional DC-DC converter

The unidirectional DC-DC converter located between PV panels and DC bus is a boost converter. When the IGBT is on, the inductance is charged by the PV systems. However, when the IGBT is turned off, then the power stored in the inductance will be released. Figure 3-2 shows the topology between PV panels and DC bus. It is worth noting that there are two diodes D₁ and D₂ which are used for preventing current from flowing back to PV panels.

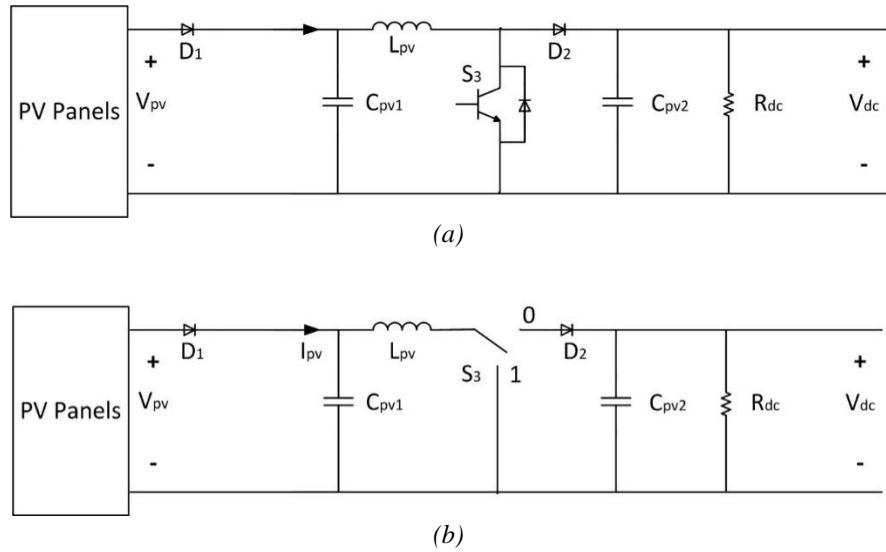


Figure 3-2 (a) The topology of the PV panels, unidirectional DC-DC converter and DC bus; (b) The equivalent circuit

If the IGBT is treated as a switch, then the circuit can be simplified as Figure 3-2 (b).

When $S_3=1$, the following circuit can be obtained:

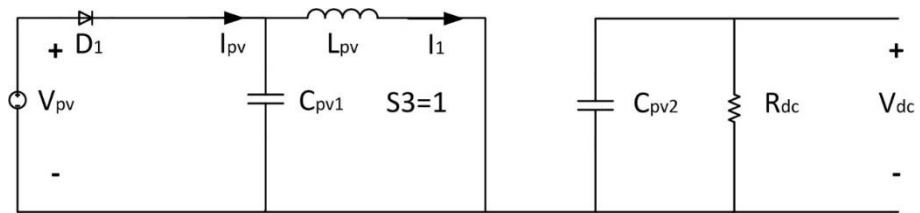


Figure 3-3 The system circuit when $S_3=1$

In this case, power is stored in the inductance. The dynamic equation of the inductance can be written as:

$$L_{pv} \frac{dI_1}{dt} = V_{pv} \quad (3-1)$$

However, when $S_3=0$, the following circuit can be obtained:

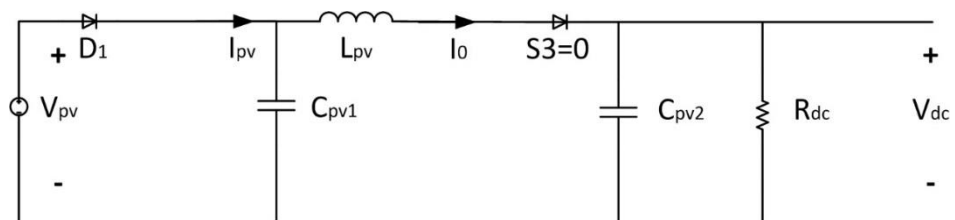


Figure 3-4 The system circuit when $S_3=0$

In this case, the power in the inductance is released and the inductance is connected with the PV panels in cascade to build up a higher voltage. The dynamic equation of the inductance then can be written as:

$$L_{pv} \frac{di_1}{dt} = V_{pv} - V_{dc} \quad (3-2)$$

Assuming that the inductance works under continuous conduction mode and the power stored in the inductance is the same amount as the power released. Then the following equation can be obtained:

$$\begin{aligned} \frac{di_0}{dt} DT + \frac{di_1}{dt} (1 - D)T &= 0 \\ \frac{V_{pv}}{L_{pv}} DT + \frac{V_{pv} - V_{dc}}{L_{pv}} (1 - D)T &= 0 \\ V_{dc} &= \frac{V_{pv}}{1 - D} \end{aligned} \quad (3-3)$$

where D and T are the duty cycle and period of the signal, respectively.

3.2.2 Modelling of the Bidirectional DC-DC Converter

Plant Specification

Figure 3-5 below shows the circuit of the battery, bidirectional DC-DC converter and how they are connected to the DC bus. The bidirectional converter is working under buck or boost mode, allowing the power to flow in or out of the battery. The control signals S_1 and S_2 are independent. When the battery is set to be charged (buck mode), then the S_2 should be kept at 0 while S_1 is switchable under two states, 0 or 1. And vice versa when the battery is discharging (boost mode). In this section, state-space equations under different cases are given to illustrate the dynamics of the circuit.

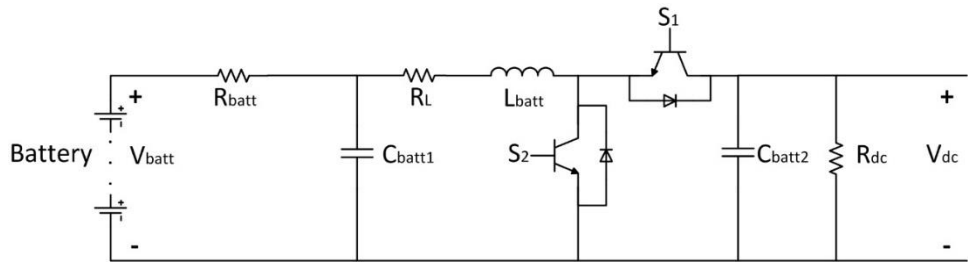


Figure 3-5 The topology of the battery, bidirectional DC-DC converter and DC bus

Buck mode

When the converter works under buck mode, S_2 is idle and S_1 is turned on or off according to cost function identified later. The voltage is stepped down from V_{dc} (voltage of DC bus) to V_{batt} (voltage of the battery) and the battery is charged by the excessive power from the DC bus. The circuit topology is then simplified as below, in which the IGBT (or MOSFET) is treated as a switch between 2 states. When $S_1=1$, the current is from the DC bus to the battery. By contrast, when $S_1=0$, then the current is through a diode to the battery. Here, the system manipulate variable $u(t)$, state $x(t)$ and output $y(t)$ are defined as below.

$$u_{buck}(t) = S_1$$

$$x_{buck}(t) = \begin{bmatrix} I_l(t) \\ V_{batt}(t) \end{bmatrix}$$

$$y_{buck}(t) = V_{batt}(t) \quad (3-4)$$

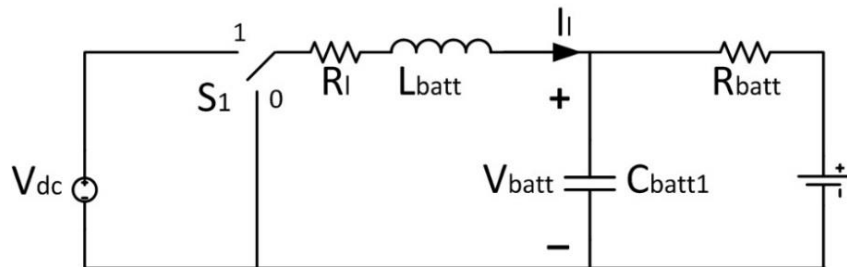


Figure 3-6 The equivalent circuit of buck mode

When $S_1=1$:

In this case, the power from the DC bus can be divided into two parts. First, some of the power is stored in the inductance L_{batt} , while the rest is used to charge the battery. From the topology shown below, the circuit dynamic can be written as equations [30]:

$$L_{batt} \frac{dI_l}{dt} = V_{dc} - V_{batt} - R_l I_l \quad (3-5)$$

$$C_{batt1} \frac{dV_{batt}}{dt} = I_l - I_{batt} = I_l - \frac{V_{batt}}{R_{batt}} \quad (3-6)$$

$$\frac{dx_{buck}(t)}{dt} = \begin{bmatrix} \frac{dI_l(t)}{dt} \\ \frac{dV_{batt}(t)}{dt} \end{bmatrix} = \begin{bmatrix} -\frac{R_l}{L_{batt}} & -\frac{1}{L_{batt}} \\ \frac{1}{C_{batt1}} & -\frac{1}{R_{batt}C_{batt1}} \end{bmatrix} \begin{bmatrix} I_l(t) \\ V_{batt}(t) \end{bmatrix} + \begin{bmatrix} \frac{1}{L_{batt}} \\ 0 \end{bmatrix} V_{dc} \quad (3-7)$$

$$y_{buck}(t) = [0 \quad 1] \begin{bmatrix} I_l(t) \\ V_{batt}(t) \end{bmatrix} \quad (3-8)$$

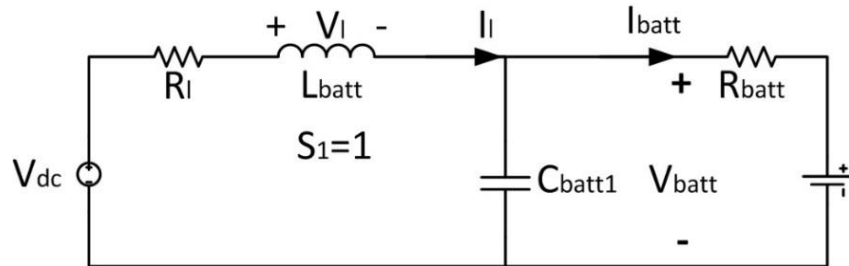


Figure 3-7 The equivalent circuit when $S_1 = 1$ (buck mode)

When $S_1=0$:

In this case, the link between DC bus and battery is disconnected. And the power stored in the inductance is released to charge the battery. With the inductance, I_l will not change dramatically when S_1 is switched from 1 to 0. The dynamic equations in this case is shown as below:

$$L_{batt} \frac{dI_l}{dt} = 0 - V_{batt} - R_l I_l \quad (3-9)$$

$$C_{batt1} \frac{dV_{batt}}{dt} = I_l - I_{batt} = I_l - \frac{V_{batt}}{R_{batt}} \quad (3-10)$$

$$\frac{dx_{buck}(t)}{dt} = \begin{bmatrix} \frac{dI_l(t)}{dt} \\ \frac{dV_{batt}(t)}{dt} \end{bmatrix} = \begin{bmatrix} -\frac{R_l}{L_{batt}} & -\frac{1}{L_{batt}} \\ \frac{1}{C_{batt1}} & -\frac{1}{R_{batt}C_{batt1}} \end{bmatrix} \begin{bmatrix} I_l(t) \\ V_{batt}(t) \end{bmatrix} \quad (3-11)$$

$$y_{buck}(t) = \begin{bmatrix} 0 & 1 \end{bmatrix} \begin{bmatrix} I_l(t) \\ V_{batt}(t) \end{bmatrix} \quad (3-12)$$

The equations acquired above are based on the assumption that the DC-DC converter works under continuous conduction mode (CCM). However, there is chance that the energy stored in the inductance is used up and the current of which stays at 0 before it is charged again by the power source. If this happens, the converter is supposed to be working under discrete conduction mode (DCM), the logic of the selection between CCM and DCM is demonstrated in Figure 3-9 and the state-space equation when $S_1=0$ can be modified as below [17]:

$$\frac{dx_{buck}(t)}{dt} = \begin{bmatrix} \frac{dI_l(t)}{dt} \\ \frac{dV_{batt}(t)}{dt} \end{bmatrix} = \begin{bmatrix} 0 & 0 \\ 0 & -\frac{1}{R_{batt}C_{batt1}} \end{bmatrix} \begin{bmatrix} I_l(t) \\ V_{batt}(t) \end{bmatrix} \quad (3-13)$$

$$y_{buck}(t) = \begin{bmatrix} 0 & 1 \end{bmatrix} \begin{bmatrix} I_l(t) \\ V_{batt}(t) \end{bmatrix} \quad (3-14)$$

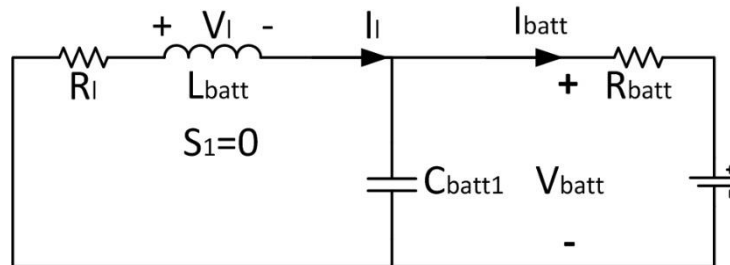


Figure 3-8 The equivalent circuit when $S_1 = 0$ (buck mode)

Assuming:

$$A_{buck_1} = \begin{bmatrix} -\frac{R_l}{L_{batt}} & -\frac{1}{L_{batt}} \\ \frac{1}{C_{batt1}} & -\frac{1}{R_{batt}C_{batt1}} \end{bmatrix}$$

$$\begin{cases} A_{buck_2} = \begin{bmatrix} 0 & 0 \\ 0 & 0 \end{bmatrix} & \text{if } I_l \neq 0 \\ A_{buck_2} = \begin{bmatrix} \frac{R_l}{L_{batt}} & \frac{1}{L_{batt}} \\ -\frac{1}{C_{batt1}} & 0 \end{bmatrix} & \text{if } I_l = 0 \end{cases}$$

$$B_{buck} = \begin{bmatrix} \frac{1}{L_{batt}} \\ 0 \end{bmatrix}$$

$$C_{buck} = [0 \quad 1]$$

Then the state-space equations for buck mode can be summarized as the equations below:

$$\frac{dx_{buck}(t)}{dt} = (A_{buck_1} + (1 - u_{buck}(t))A_{buck_2})x(t) + B_{buck}u_{buck}(t)V_{dc} \quad (3-15)$$

$$y_{buck}(t) = C_{buck}x(t) \quad (3-16)$$

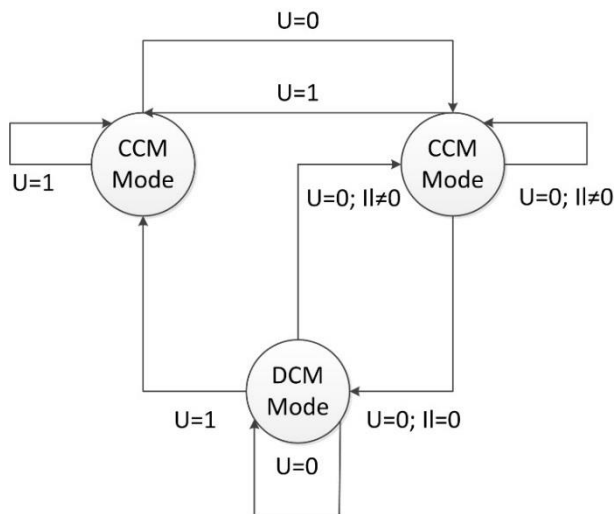


Figure 3-9 The logic of conduction mode selection

Boost mode

Comparing with the buck mode, the S_1 is kept constantly zero in the boost mode. By changing S_2 to 0 or 1, the voltage is stepped up from V_{batt} to V_{dc} and the battery is discharging. When $S_2=1$, the IGBT is turned on and the current cannot reach the DC bus. However, when $S_2=0$, the IGBT is turned off and the current will go through the diode to the DC bus. The manipulate variable $u(t)$, state $x(t)$ and output $y(t)$ for boost mode are defined as below:

$$u_{boost}(t) = S_2$$

$$x_{boost}(t) = \begin{bmatrix} I_l(t) \\ V_{dc}(t) \end{bmatrix}$$

$$y_{boost}(t) = V_{dc}(t)$$

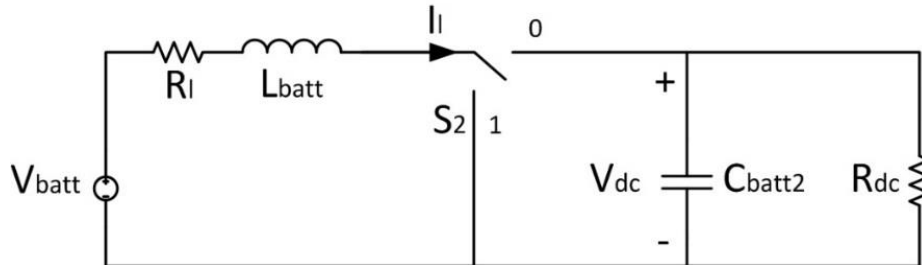


Figure 3-10 The equivalent circuit of boost mode

When $S_2=1$:

In this case, the whole circuit is divided into two separated parts. The inductance is charged up by the battery. The circuit dynamic equation can be written as below:

$$L_{batt} \frac{dI_l}{dt} = V_{batt} - R_l I_l \quad (3-17)$$

$$C_{batt2} \frac{dV_{dc}}{dt} = 0 - I_{dc} = -\frac{V_{dc}}{R_{dc}} \quad (3-18)$$

$$\frac{dx_{boost}(t)}{dt} = \begin{bmatrix} \frac{dI_l(t)}{dt} \\ \frac{dV_{dc}(t)}{dt} \end{bmatrix} = \begin{bmatrix} -\frac{R_l}{L_{batt}} & 0 \\ 0 & -\frac{1}{R_{dc}C_{batt2}} \end{bmatrix} \begin{bmatrix} I_l(t) \\ V_{dc}(t) \end{bmatrix} + \begin{bmatrix} \frac{1}{L_{batt}} \\ 0 \end{bmatrix} V_{batt} \quad (3-19)$$

$$y_{boost}(t) = [1 \quad 0] \begin{bmatrix} I_l(t) \\ V_{dc}(t) \end{bmatrix} \quad (3-20)$$

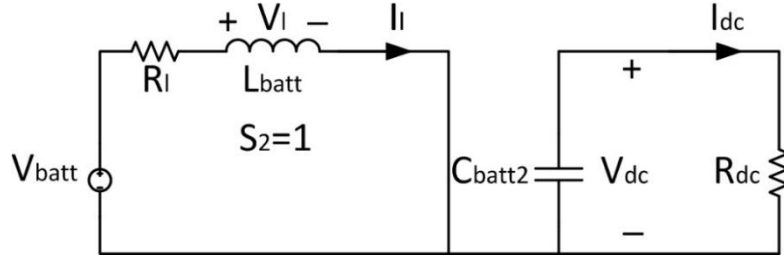


Figure 3-11 The equivalent circuit when $S_2 = 1$ (boost mode)

When $S_2=0$:

The link between battery side and DC bus side will recover. The inductance will release the stored power and be connected with the battery in cascade to deliver power to the DC bus. In this case, the dynamic equations (under CCM) are:

$$L_{batt} \frac{dI_l}{dt} = V_{batt} - V_{dc} - R_l I_l \quad (3-21)$$

$$C_{batt2} \frac{dV_{dc}}{dt} = I_l - I_{dc} = I_l - \frac{V_{dc}}{R_{dc}} \quad (3-22)$$

$$\frac{dx_{boost}(t)}{dt} = \begin{bmatrix} \frac{dI_l(t)}{dt} \\ \frac{dV_{dc}(t)}{dt} \end{bmatrix} = \begin{bmatrix} -\frac{R_l}{L_{batt}} & -\frac{1}{L_{batt}} \\ \frac{1}{C_{batt2}} & -\frac{1}{R_{dc}C_{batt2}} \end{bmatrix} \begin{bmatrix} I_l(t) \\ V_{dc}(t) \end{bmatrix} + \begin{bmatrix} \frac{1}{L_{batt}} \\ 0 \end{bmatrix} V_{batt} \quad (3-23)$$

$$y_{boost}(t) = [1 \quad 0] \begin{bmatrix} I_l(t) \\ V_{dc}(t) \end{bmatrix} \quad (3-24)$$

If the converter operates under DCM, then the state-space equations can be rewritten as:

$$\frac{dx_{boost}(t)}{dt} = \begin{bmatrix} \frac{dI_l(t)}{dt} \\ \frac{dV_{dc}(t)}{dt} \end{bmatrix} = \begin{bmatrix} 0 & 0 \\ 0 & -\frac{1}{R_{dc}C_{batt2}} \end{bmatrix} \begin{bmatrix} I_l(t) \\ V_{dc}(t) \end{bmatrix} + \begin{bmatrix} \frac{1}{L_{batt}} \\ 0 \end{bmatrix} V_{batt} \quad (3-25)$$

$$y_{boost}(t) = [1 \quad 0] \begin{bmatrix} I_l(t) \\ V_{dc}(t) \end{bmatrix} \quad (3-26)$$

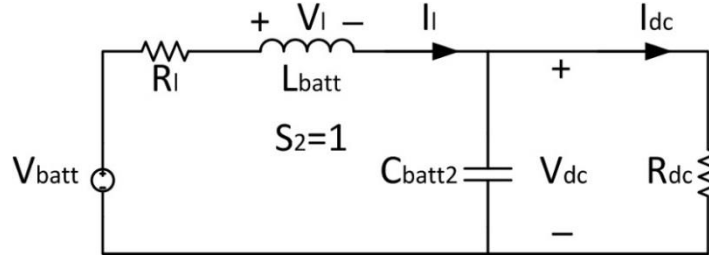


Figure 3-12 The equivalent circuit when $S_2 = 0$ (boost mode)

Assuming:

$$\begin{cases} A_{boost_1} = \begin{bmatrix} -\frac{R_l}{L_{batt}} & -\frac{1}{L_{batt}} \\ \frac{1}{C_{batt2}} & -\frac{1}{R_{dc}C_{batt2}} \end{bmatrix} & \text{if } I_l \neq 0 \\ A_{boost_1} = \begin{bmatrix} 0 & 0 \\ 0 & -\frac{1}{R_{dc}C_{batt2}} \end{bmatrix} & \text{if } I_l = 0 \end{cases}$$

$$\begin{cases} A_{boost_2} = \begin{bmatrix} 0 & \frac{1}{L_{batt}} \\ -\frac{1}{C_{batt2}} & 0 \end{bmatrix} & \text{if } I_l \neq 0 \\ A_{boost_2} = \begin{bmatrix} -\frac{R_l}{L_{batt}} & 0 \\ 0 & 0 \end{bmatrix} & \text{if } I_l = 0 \end{cases}$$

$$\begin{cases} B_{boost} = \begin{bmatrix} \frac{1}{L_{batt}} \\ 0 \end{bmatrix} & \text{if } I_l \neq 0 \\ B_{boost} = \begin{bmatrix} 0 \\ 0 \end{bmatrix} & \text{if } I_l = 0 \end{cases}$$

$$C_{boost} = [1 \quad 0]$$

Then the state-space equations for boost mode can be summarized as the equations below:

$$\frac{dx_{boost}(t)}{dt} = (A_{boost_1} + u_{boost}(t)A_{boost_2})x(t) + B_{boost}V_{batt} \quad (3-27)$$

$$y_{boost}(t) = C_{boost}x(t) \quad (3-28)$$

3.3 Controlling Design for the Integrated PV Solar and Battery System

According to different amount of solar PV power output and the state of charge of the battery, the systems can be identified as working under two different modes:

Mode I (normal mode):

$$P_{pv} < P_L \text{ and } SOC > SOC_{min}$$

or

$$P_{pv} > P_L \text{ and } SOC < SOC_{max}$$

where P_{pv} , P_L are the PV power output and power consumption, respectively. SOC, SOC_{min} and SOC_{max} are battery state of charge, the minimum state of charge and the maximum state of charge. In these two cases, the unidirectional converter will work under MPPT mode to exact maximum power from solar panels, while the bidirectional converter will work under MPC mode to charge or discharge the battery accordingly.

Mode II (idle mode):

$$P_{pv} < P_L \text{ and } SOC < SOC_{min}$$

or

$$P_{pv} > P_L \text{ and } SOC > SOC_{max}$$

In this case, the battery will be disconnected with the whole circuit to avoid overdischarging or overcharging. Without the battery, the DC bus voltage cannot be maintained within a certain range and the excessive/deficit power cannot be absorbed/compensated. Therefore, the PV panels are also disconnected to protect the load from any potential damage.

This research focus on Mode I, in which the battery can fulfil the responsibility of stabilizing the DC bus voltage and balancing power within the hybrid system.

3.3.1 Controlling Design for the Unidirectional DC-DC Converter

Maximum power point tracking (MPPT) algorithm is one of the most popular controlling methods for PV panels' controlling. As its name indicated, this method is applied to extract the maximum power from solar system by shifting the output voltage of the PV panels according to the amount of sun power/solar irradiance received. Once the converter output side is linked to a DC bus, the output voltage is assumed to be just varied in a small range (or assuming the voltage of the DC bus is fixed). By changing the duty cycle, the input side voltage from PV module is changed accordingly. The MPPT controlling strategy used in this research is based on perturb and observe nature. Small voltage increase or decrease is imposed upon the solar panels and the power output change is measured. Then the derivative of power over voltage is compared with 0, which decides how the operation point moves. Here, the Incremental Conductance Based Maximum Power Point Tracking is illustrated below.

The P-V curve of the BP solar SX3190, which is used for simulation, is shown in Figure 3-13. When

$$\frac{dP}{dV} = 0$$

At MPPT (lock the duty cycle as a constant). See the point 1.

$$\frac{dP}{dV} > 0$$

Left of MPPT (corresponding solution, decrease the duty cycle D of the unidirectional converter, then the output voltage of PV module is stepped up). See the point 2.

$$\frac{dP}{dV} < 0$$

Right of MPPT (corresponding solution, increase the duty cycle D of the unidirectional converter, then the output voltage of PV module is stepped down). See the point 3.

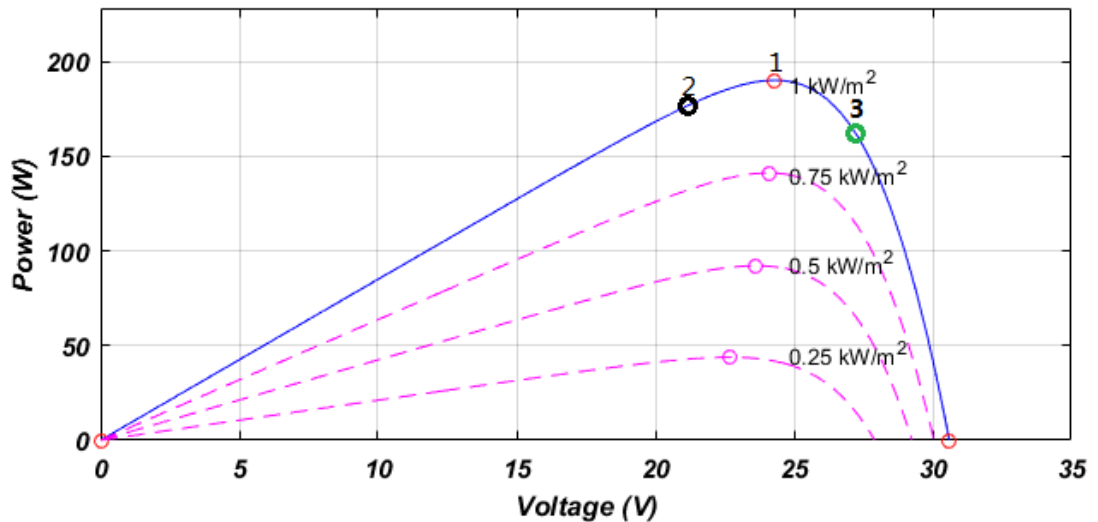


Figure 3-13 P-V curve of BP Solar SX3190 under different solar irradiance

However, in order to find out the maximum power point, the comparison between dp/dv and 0 is replaced by a more straightforward method-by comparing the dI/dV and I/V . As it is known that:

$$P = VI \tag{3-29}$$

$$\frac{dP}{dV} = \frac{d(VI)}{dV} = I + V \frac{dI}{dV} \tag{3-30}$$

Therefore, the three situations listed above can be modified by substituting $I+V^*(dI/dV)$ to dP/dV .

$$\frac{dI}{dV} = -\frac{I}{V} \text{ (For continuous mode) or } \frac{\Delta I}{\Delta V} = -\frac{I}{V} \text{ (For discrete mode)}$$

$$\frac{dI}{dV} > -\frac{I}{V} \text{ (For continuous mode) or } \frac{\Delta I}{\Delta V} > -\frac{I}{V} \text{ (For discrete mode)}$$

$$\frac{dI}{dV} < -\frac{I}{V} \text{ (For continuous mode) or } \frac{\Delta I}{\Delta V} < -\frac{I}{V} \text{ (For discrete mode)}$$

The three equations above indicate the PV panels are working under maximum power point, left of the maximum power point and right of the maximum power point, respectively. The process of moving the operation point towards maximum power point is shown in Figure 3-14 below:

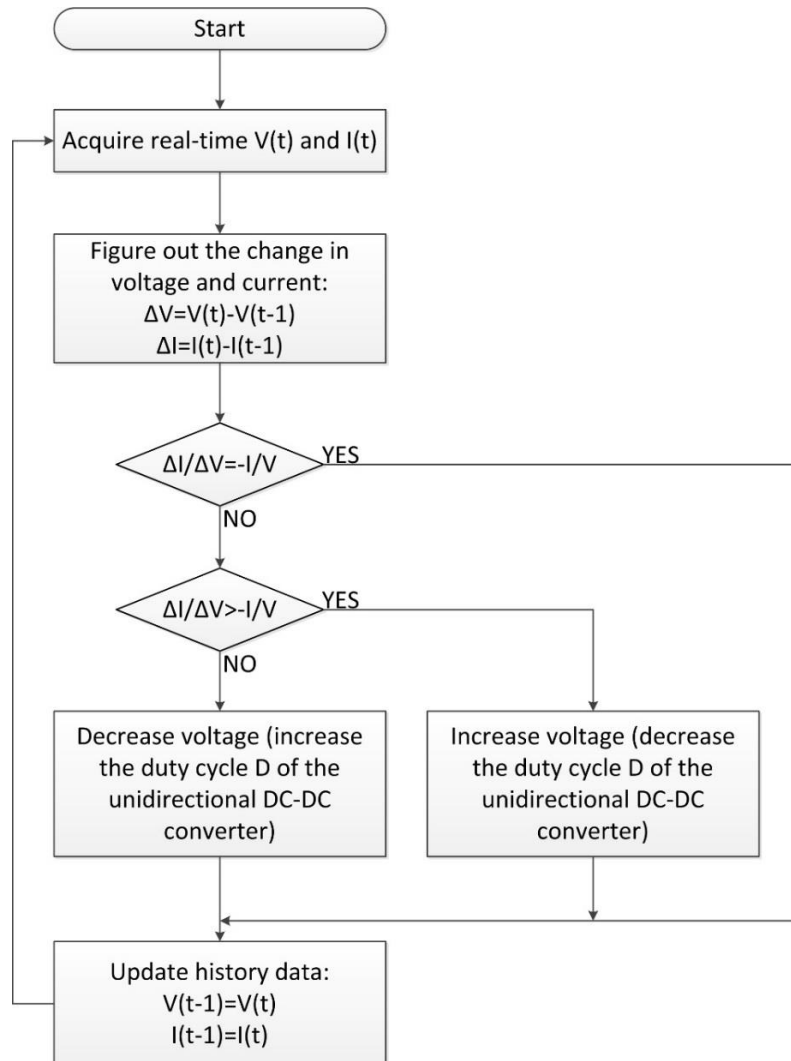


Figure 3-14 The logic of the MPPT algorithm

3.3.2 Controlling Design for the Bidirectional DC-DC Converter

Basics of Model Predictive Control

Model Predictive Control (MPC) is basically an open loop optimization algorithm based on the receding horizon principle. Normal open-loop optimization algorithm uses one temporal horizon for both prediction and controlling. This may end up with problems like hitting the system constraints as the duration of control window extends. However, by

setting the prediction horizon and controlling horizon separately (normally a larger prediction horizon), the open-loop control period can be effectively decreased and the problems can be avoided.

Assuming that we have u and y representing the system input and output signal and y_{ref} is the reference value of output. First, according to the initial value and reference value of the system output, the optimal problem is solved for a certain time interval, which is also known as prediction horizon. A sequence of future control signals U then can be computed and those with the aim of minimizing the performance index for the prediction horizon (in this case, minimizing the gap between real-time value and reference value of the battery terminal voltage) and avoiding violating the system constraints are figured out. However, MPC algorithm is not using all the input signals from the last step, only the first few values of U are set as the plant input and implemented for a smaller time interval, which is defined as control horizon. It is worth noting that control horizon should be set shorter than prediction horizon and that is why this principle is called receding horizon principle. At the end of every control horizon, the control signals which are not implemented are discarded and the whole procedure is repeated [38].

Model Predictive Control for the Bidirectional DC-DC Converter

State and output anticipation

Real-time measurement is conducted during every single sample time. As a stand-alone system, the voltage of DC bus is critical for system operation and should be maintained within a certain range. Therefore, the voltage threshold of DC bus for shifting states of the bidirectional converter are set. The working condition of the bidirectional converter,

according to the real time V_{dc} values, is shifted to balance the power generated and consumed. Table below shows the logic of the bidirectional DC-DC converter.

V_{dc}	The state of bidirectional DC-DC converter
<100V	Boost (Discharge)
100V-102V	Idle
>102V	Buck (Charge)

Table 3-1 The voltage threshold for different converter states

Once the operation mode of the converter is determined, the corresponding state-space equation used for predicting is then confirmed. Continuous state-space equations are given in the last section. According to those, the discrete state-space equations can be obtained by using the 'c2d' function in Matlab. Since there are two situations (corresponding to IGBT on or off) in both buck mode and boost mode, 4 different discrete state-space equations are required to show the whole possible dynamic of the system.

Table 3-1 below shows the 4 situations according to the converter modes and the IGBT status.

Mode	S_1	S_2	Situation Number (n)
Buck	1	0	1
	0	0	2
Boost	0	1	3
	0	0	4

Table 3-2 Different situation numbers for different modes

Assume we have:

Buck mode (n=1 or 2):

$$x(t + 1) = E_n x(t) + F_n V_{dc} \quad (3-31)$$

$$y(t) = G_n x(t) \quad (3-32)$$

Boost mode (n=3 or 4):

$$x(t + 1) = E_n x(t) + F_n V_{batt} \quad (3-33)$$

$$y(t) = G_n x(t) \quad (3-34)$$

where E_n , F_n and G_n are the parameters of discrete state-space equations in different situations (n is the situation number).

The state and output anticipations are based on those four sets of equations. For example, if the converter works under buck mode and the first, second and third values of S_1 are 1, 0 and 0, respectively.

Then $x(t+1)$ can be derived as:

$$x(t + 1) = E_1 x(t) + F_1 V_{dc} \quad (3-35)$$

$$y(t) = G_1 x(t) \quad (3-36)$$

$x(t+2)$ can be derived as:

$$x(t + 2) = E_2 x(t + 1) + F_2 V_{dc} \quad (3-37)$$

$$y(t + 1) = G_1 x(t + 1) \quad (3-38)$$

$x(t+3)$ can be derived as:

$$x(t + 3) = E_2 x(t + 2) + F_2 V_{dc} \quad (3-39)$$

$$y(t + 2) = G_1x(t + 2) \quad (3-40)$$

Combining the equations above, then we can get the prediction of $x(t+3)$ based on the latest measurement $x(t)$ and V_{dc} , which is shown as below:

$$\begin{aligned} x(t + 3) &= E_2(E_2(E_1x(t) + F_1V_{dc}) + F_2V_{dc}) + F_2V_{dc} = E_2(E_2E_1x(t) + (E_2F_1 + \\ &F_2)V_{dc}) + F_2V_{dc} = E_2^2E_1x(t) + (E_2^2F_1 + E_2F_2 + F_2)V_{dc} \end{aligned} \quad (3-41)$$

$$y(t + 2) = G_1(E_2(E_1x(t) + F_1V_{dc}) + F_2V_{dc}) = G_1E_2E_1x(t) + (G_1E_2F_1 + G_1F_2)V_{dc} \quad (3-42)$$

If the converter works under boost mode and the first, second and third value of S_2 are 1, 0 and 0. Then as what has been achieved in the buck mode illustrated above, the corresponding state and output should be:

$$x(t + 3) = E_4^2E_3x(t) + (E_4^2F_3 + E_4F_4 + F_4)V_{batt} \quad (3-43)$$

$$y(t + 2) = G_3E_4E_3x(t) + (G_3E_4F_3 + G_3F_4)V_{batt} \quad (3-44)$$

This is not just restricted to 3-step-ahead prediction. The same theory can be applied to m -step-ahead prediction. However, the more steps anticipated, the more calculation is required which may increase the response time of computing.

Defining cost function

The main goal of the control part of this study is to balance the power generation and power consumption by charging/discharging the battery. To be more exact, the voltage of the battery is controlled in this study, which allows the battery to absorb/supply power from/to the DC bus.

When the converter operates under buck mode which means the power generation from PV panels exceeds the power consumption of the load, the voltage of the DC bus is stepped down and the battery is charged. The power balance equation should be:

$$P_{charge} + P_{circuit} + P_{load} = P_{panels} \quad (3-45)$$

where, P_{charge} , $P_{circuit}$, P_{load} and P_{panels} are the power used to charge the battery, the power consumed by the circuit, the power provided to the load and the power generation from the PV panels, respectively.

Figure 3-15 shows a simplified battery model used in this study and its external wiring. From that, the following equations can be obtained:

$$I_{batt} = \frac{E_{batt} - V_{batt}}{R_{batt}} \quad (3-46)$$

$$P_{circuit} = I_l^2 R_l \quad (3-47)$$

$$P_{charge} = V_{batt} I_l \quad (3-48)$$

where E_{batt} is the constant electromotive force, which is 50V in this case. I_{batt} and I_l is the battery internal and external currents, respectively.

In order to simplified this problem further, a relatively large capacitance is used which make I_{batt} roughly of the same value as I_l . Therefore, assuming $I_{batt} = I_l$ and combining equations (3-45) to (3-48), the power balance equation can be modified as below:

$$\frac{E_{batt} - V_{batt}}{R_{batt}} V_{batt} + \left(\frac{E_{batt} - V_{batt}}{R_{batt}} \right)^2 R_l = P_{panels} - P_{load} \quad (3-49)$$

By solving the quadratic equation (3-49), the voltage reference of the battery can be derived.

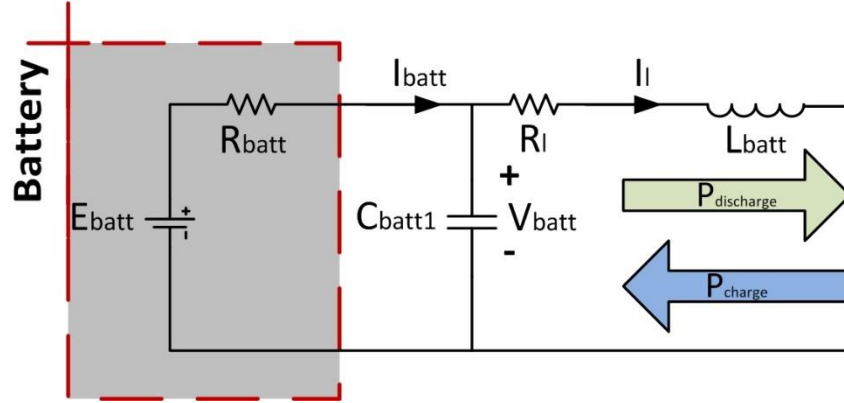


Figure 3-15 The simplified battery model

In boost mode, the power balance equation should be:

$$P_{discharge} + P_{panels} = P_{circuit} + P_{load} \quad (3-50)$$

Using the same approximation in buck mode, the voltage reference can be derived by solving the quadratic equation below:

$$\frac{E_{batt} - V_{batt}}{R_{batt}} V_{batt} + P_{panels} = \left(\frac{E_{batt} - V_{batt}}{R_{batt}} \right)^2 R_l + P_{load} \quad (3-51)$$

The system output y in buck mode is the voltage of the battery (V_{batt_p}) while that in boost mode is the external current (I_{l_p}). However, for both situations, the reference values should be the voltage of the battery. Therefore, in boost mode, the current prediction is transformed to battery voltage prediction by combining equation (3-46) and the same approximation ($I_{batt_p} = I_{l_p}$) mentioned above:

$$V_{batt_p} = E_{batt} - I_{l_p} R_{batt} \quad (3-52)$$

where V_{batt_p} and I_{l_p} are the anticipated values of terminal voltage of the battery and external current, respectively.

The cost function, which is the main criterion to decide how the converter works, can be defined as the gap between predicted values and desired values. Assume V_{batt_r} to be the reference in both buck and boost modes, then the cost function can be defined as below:

$$J = \sum_{i=1}^{H_p} |V_{batt_r} - V_{batt_p}(k+i|k)| \quad (3-53)$$

where H_p is the prediction horizon, $V_{batt_p}(k+i|k)$ is the prediction of battery terminal voltage at time $k+i$ based on the measurement at time k .

In this research, the prediction horizon is 3 steps ahead. The cost function is calculated at every sample time depending on the values of S_1 and S_2 . All the possible situations under buck/boost mode are listed in Figure 3-16. One thing worth noting is that the reference values, both V_{dc_r} and V_{batt_r} are assumed to be constant when calculating the three-step-accumulating cost function. This is because the sample time is set to be much smaller than the update cycle of solar irradiance prediction. So the equations above should be modified as follow:

Under buck mode,

$$J_{buck} = J_1 + J_2 + J_3 = |V_{batt_r} - y_t| + |V_{batt_r} - y_{t+1}| + |V_{batt_r} - y_{t+2}| \quad (3-54)$$

Under boost mode,

Set:

$$y'_t = E_{batt} - R_{batt}y_t \quad (3-55)$$

$$J_{boost} = J_1 + J_2 + J_3 = |V_{batt_r} - y'_t| + |V_{batt_r} - y'_{t+1}| + |V_{batt_r} - y'_{t+2}| \quad (3-56)$$

where J_1 , J_2 and J_3 are the cost function values for the first, second and third step.

In Table 3-3 The anticipating actions of the IGBT in a prediction horizon and its corresponding cost function values, cost functions for different on and off sequence of the corresponding IGBT are presented. There are eight cases under either buck or boost mode and by comparing them, the minimum cost function values are found out.

$$J_{buck_min} = \min\{J_{S1_1}, J_{S1_2}, \dots, J_{S1_8}\} \quad (3-57)$$

$$J_{boost_min} = \min\{J_{S2_1}, J_{S2_2}, \dots, J_{S2_8}\} \quad (3-58)$$

Although three control variables are derived every time the minimum cost function is figured out, just the first control variable will be applied to the process. As this is based on rolling optimal process, the same procedure repeats at every single sample time.

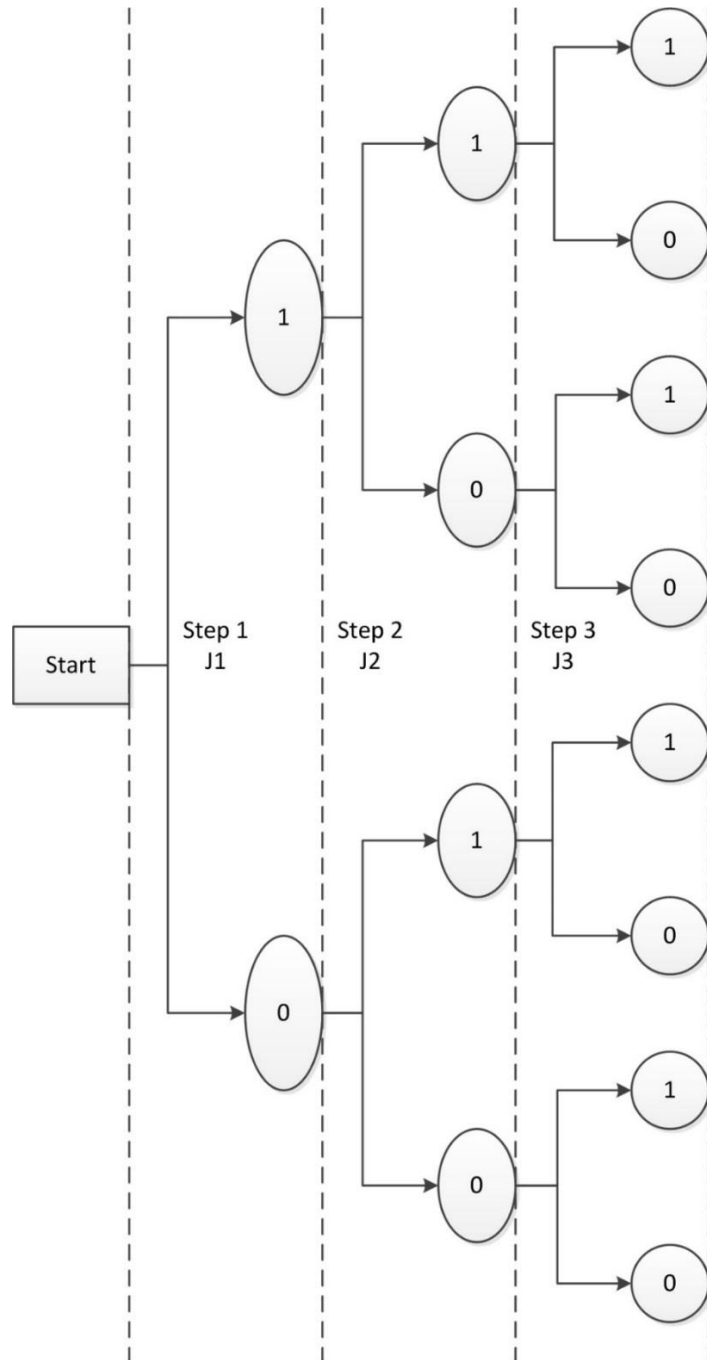


Figure 3-16 The possible values sequence of a single IGBT in buck or boost mode (0-off; 1-on)

Buck mode	Values Sequence	J1+J2+J3	Boost mode	Values Sequence	J1+J2+J3
S1	0,0,0	J_S1_1	S2	0,0,0	J_S2_1
	0,0,1	J_S1_2		0,0,1	J_S2_2
	0,1,0	J_S1_3		0,1,0	J_S2_3
	0,1,1	J_S1_4		0,1,1	J_S2_4
	1,0,0	J_S1_5		1,0,0	J_S2_5
	1,0,1	J_S1_6		1,0,1	J_S2_6
	1,1,0	J_S1_7		1,1,0	J_S2_7
	1,1,1	J_S1_8		1,1,1	J_S2_8

Table 3-3 The anticipating actions of the IGBT in a prediction horizon and its corresponding cost function values

Chapter 4 Results

In this section, the MPC control algorithm is tested by applying solar irradiance prediction. Figure 4-1 shows the solar irradiance measurement of the Black Mountain site. The measurement data is with time resolution of 1s. Instead of simulating the whole period, just the data of interest which is located in the rectangular box is selected to inspect the feasibility and effectiveness of the control algorithm. Obviously, the fluctuation of solar irradiance poses a challenge to the controller, while the relatively stable solar isolation is easier for the controller to cope with. The highlighted data inside the dashed rectangle shows a large fluctuation, which was probably caused by a small moving cloud.

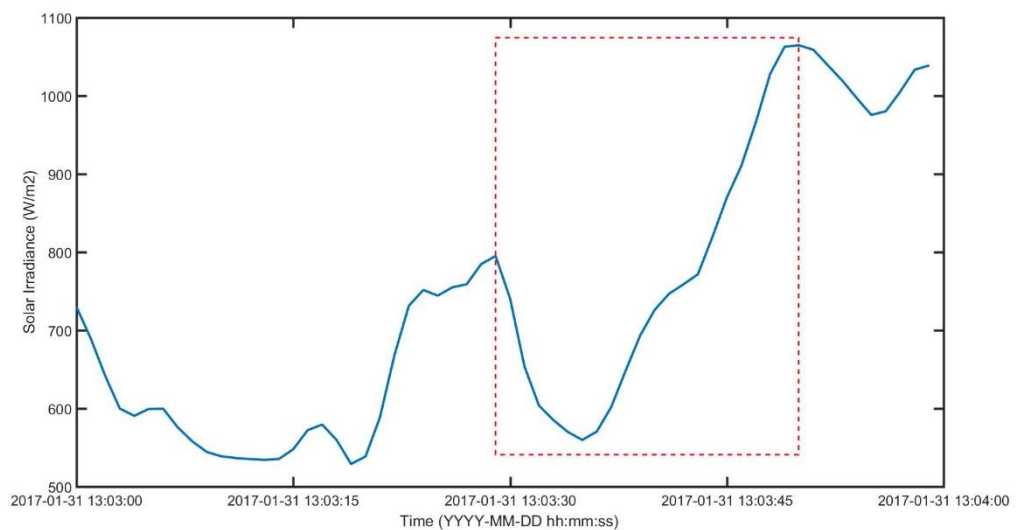


Figure 4-1 The solar irradiance measurement of Black Mountain site from 31-01-2017 13:03:00 to 31-01-2017 13:03:59

The dashed rectangular box highlights the data of interest and Table 4-1 shows the second by second measurement of solar irradiance. The reason for selecting this is because the feasibility and effectiveness of both the solar insolation prediction and the controlling algorithm need to be tested under such a huge fluctuation. As can be seen, the insolation

drops from about 800 W/m² to 550 W/m², which is the lowest value point. After that, the irradiance becomes increasingly stronger and hits over 1050 W/m² at the end of the selected period.

Time	Date, Hour and Minute	2017-01-31 13:03							
	Second	29	30	31	32	33	34	35	36
Measurement value(W/m ²)		795.2	740.9	653.7	603.7	585.1	570.0	559.7	570.4
Time	Date, Hour and Minute	2017-01-31 13:03							
	Second	37	38	39	40	41	42	43	44
Measurement value(W/m ²)		601.7	648.4	693.2	725.9	746.7	758.8	771.7	819.2
Time	Date, Hour and Minute	2017-01-31 13:03							
	Second	45	46	47	48	49	50		
Measurement value(W/m ²)		910.1	965.7	1028.0	1062.7	1064.7	965.7		

Table 4-1 The solar irradiance measurement data from 31-01-2017 13:03:29 to 31-01-2017 13:03:50

Assuming every solar irradiance value remains the same for one second until the next measurement is updated, the change of the solar irradiance can be demonstrated as Figure 4-2. In order to simplify the ‘time’ label, in Figure 4-2, ‘29’ represents the time ‘31-01-2017 13:03:29’, ‘31’ represents the time ‘31-01-2017 13:03:31’ and so on.

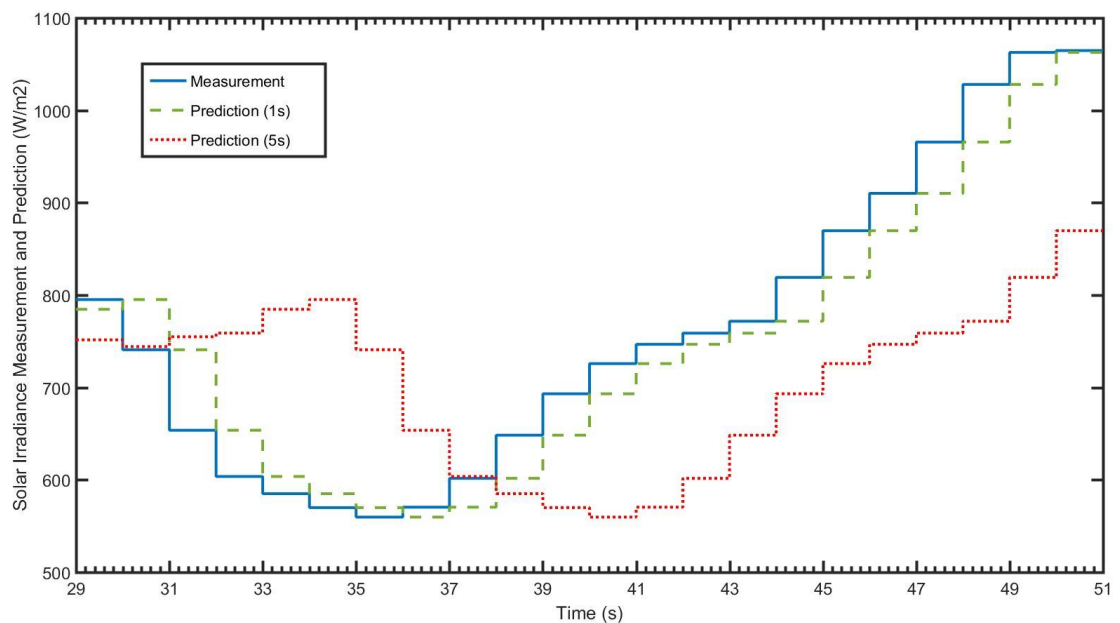


Figure 4-2 The change in the measurement and prediction during the selected period

As discussed in the previous section, the higher the resolution of the solar irradiance, the better the persistence model performs. Therefore, in order to demonstrate how the prediction accuracy affects the overall control quality, prediction results of applying the persistence algorithm (with lead time of 1s and 5s) are used in this section. In Figure 4-2, the blue signal will be used as the input of the solar PV panels. At the same time, the controller is deployed by using solar irradiance prediction (the dashed and dotted signals). The logic is demonstrated in Figure 4-3.

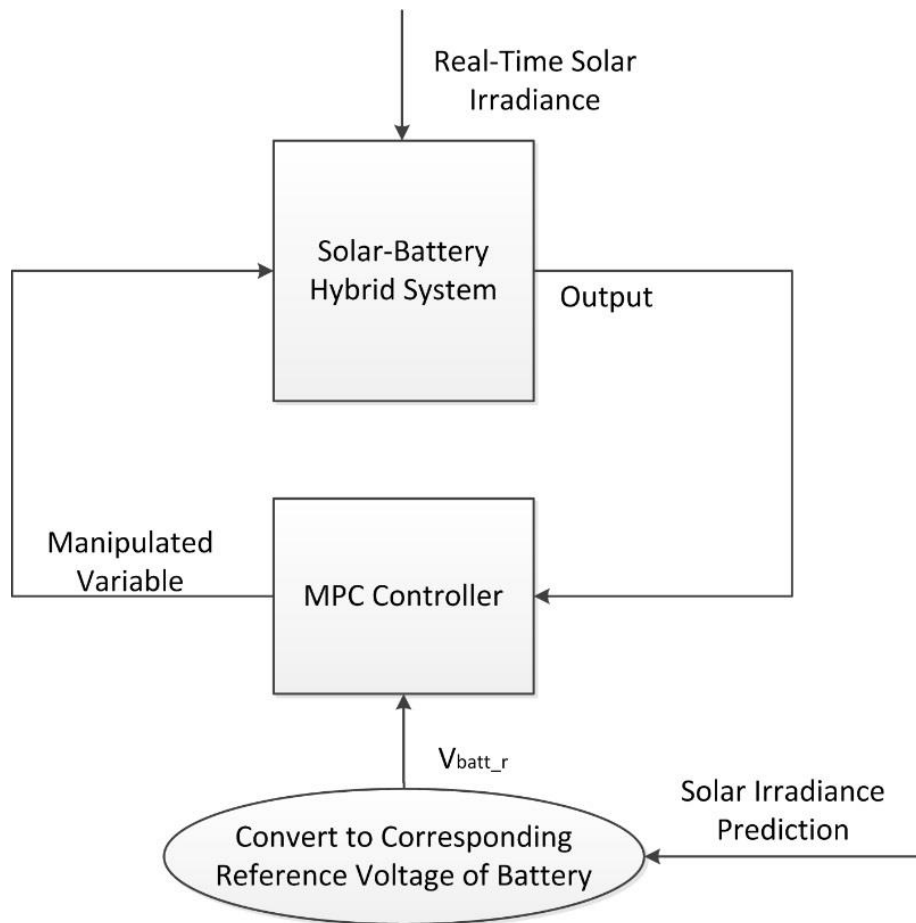


Figure 4-3 The logic of the operation

From the previous section, it is known that prediction with shorter lead-time is more accurate than that with longer lead time. In this section, the forecast performance is further

evaluated in the proposed PV-Battery Hybrid system to emphasize the importance of anticipation accuracy to the controller deployment.

Figure 4-4 shows the voltage against time of the DC bus by using solar irradiance prediction with lead time of 1s. It can be seen that the average voltage is successfully maintained at $100V \pm 5V$ even though there are some small spikes. Figure 4-5 illustrates how control signals S1 and S2 change according to different solar insolation values. From 29s to 32s, S2 is constantly at 0 while S1 was switchable. It indicates that the DC-DC Buck-Boost converter is deployed as a buck converter, which means the battery is set to be charged. From 32s to 33s, both the signal values remain at 0. The converter is idle. However, from Figure 4-4, it is clear that the voltage dropped from 102V to 95V, which means that the real-time solar irradiance is lower than the anticipation. Instead of being idle, discharging the battery would be a more proper action for the converter. From 33s to 36s, it seems that the solar irradiance is still overestimated. As a result, not enough battery power is fed in the DC bus though the voltage is still within the predefined range and getting closer and closer to the perfect value, 100V.

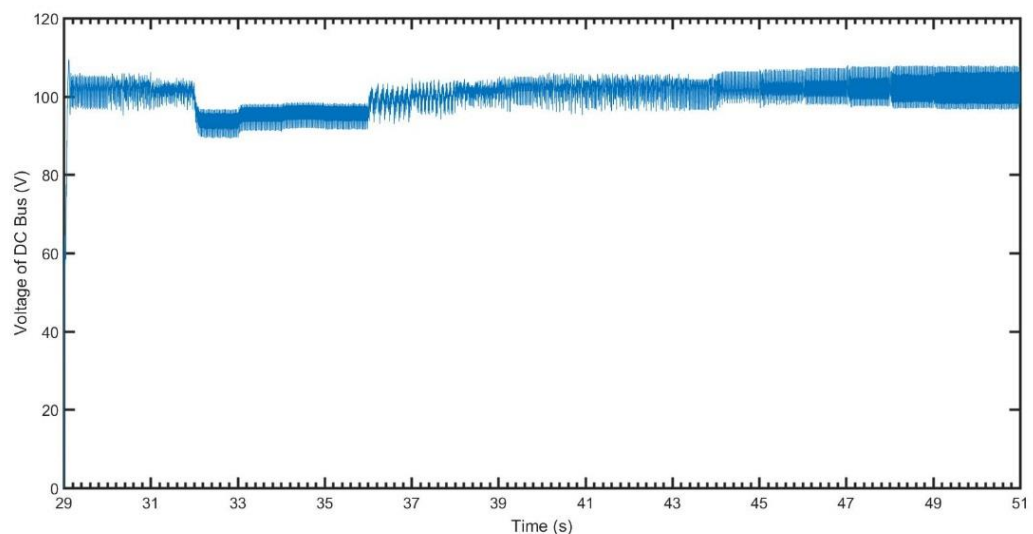


Figure 4-4 The voltage of DC bus (prediction horizon time: 1s)

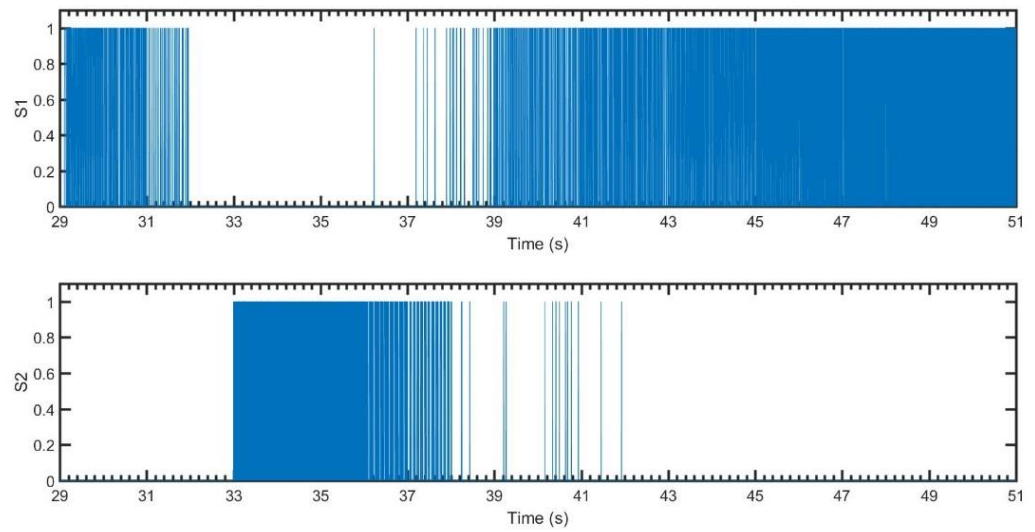


Figure 4-5 The values of control signals ($S1$ and $S2$) (prediction horizon time: 1s)

Figure 4-6 and Figure 4-7 show the current and voltage of the battery, and how the power of different components of the hybrid system change. Due to the relatively stable voltage of DC bus, the power consumption is stabilized at roughly 400W during the whole simulation period. However, the power consumed or supplied by the battery is changed as the solar power varies.

Results show that when using the solar irradiance prediction with lead-time of 1 second, the voltage of the DC bus could be maintained within a satisfactory range. Besides, the converter could fulfil the function of balancing power supply and power consumption quite well.

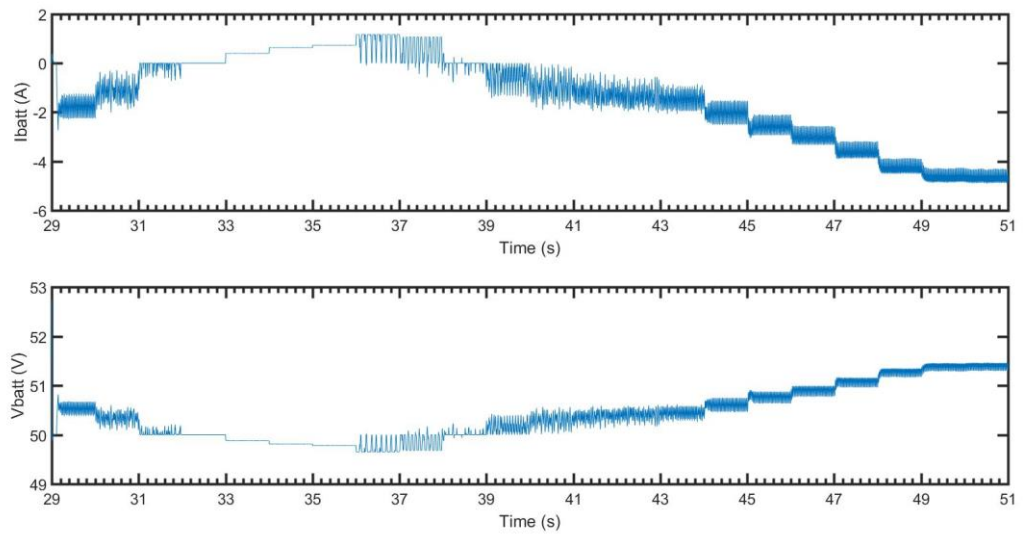


Figure 4-6 The current and voltage of the battery (prediction horizon time: 1s)

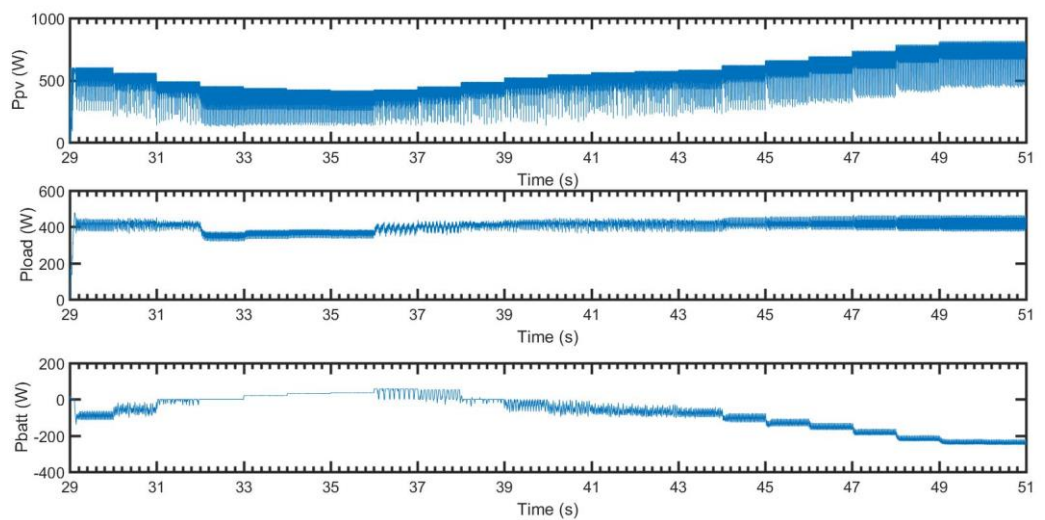


Figure 4-7 The power change of pv panels, load and battery (prediction horizon time: 1s)

If the horizon time of prediction extends, the performance of the system will deteriorate. For comparison, the prediction with lead time of 5 second is used for demonstration. Figure 4-8 - Figure 4-11 show the voltage of DC bus, how S1 and S2 operate, the current and voltage of the battery and the power dynamic of the PV panels, Load and the storage. When compared with the case where lead time is 1s, it is obvious that the voltage is not as stable, especially from 32-38s, the voltage dropped under 95V and deteriorated as the solar irradiance decreased. With the lower prediction accuracy, the bidirectional converter

is set to be idle from 32-37s and the power from the battery, therefore, is not injected to the DC bus in time. However, in the case using lead time of 1s, the response of the battery is much faster and the voltage of the DC bus could be maintained effectively.

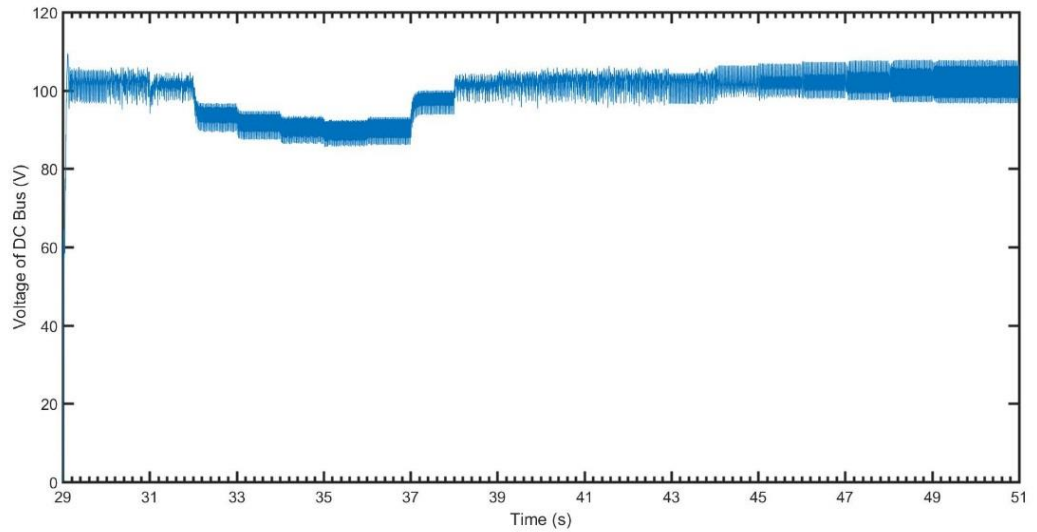


Figure 4-8 The voltage of DC bus (prediction horizon time: 5s)

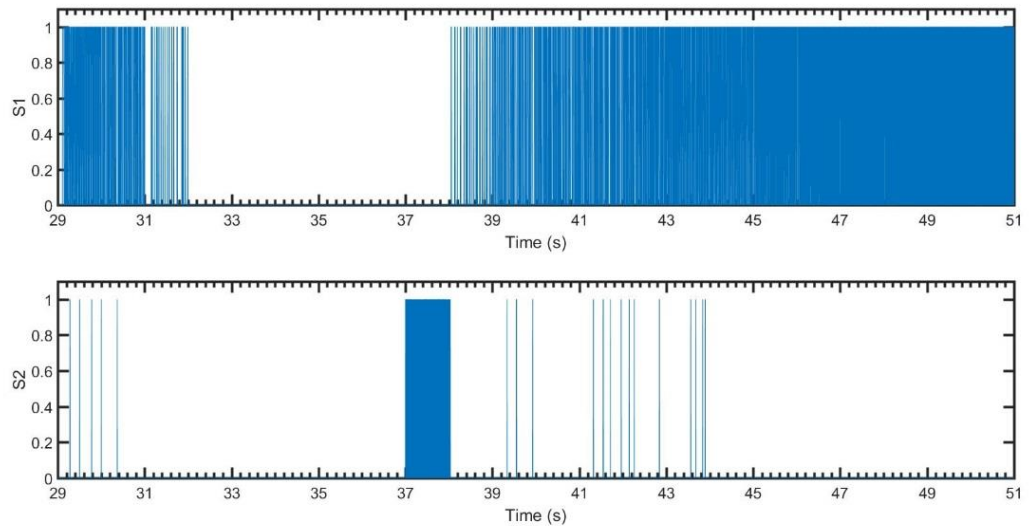


Figure 4-9 The values of control signals (S1 and S2) (prediction horizon time: 5s)

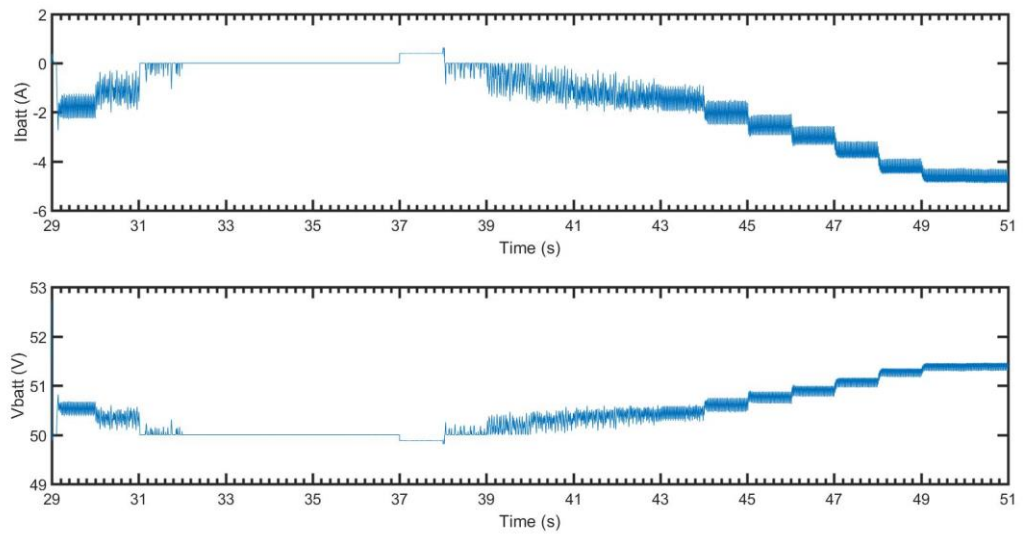


Figure 4-10 The current and voltage of the battery (prediction horizon time: 5s)

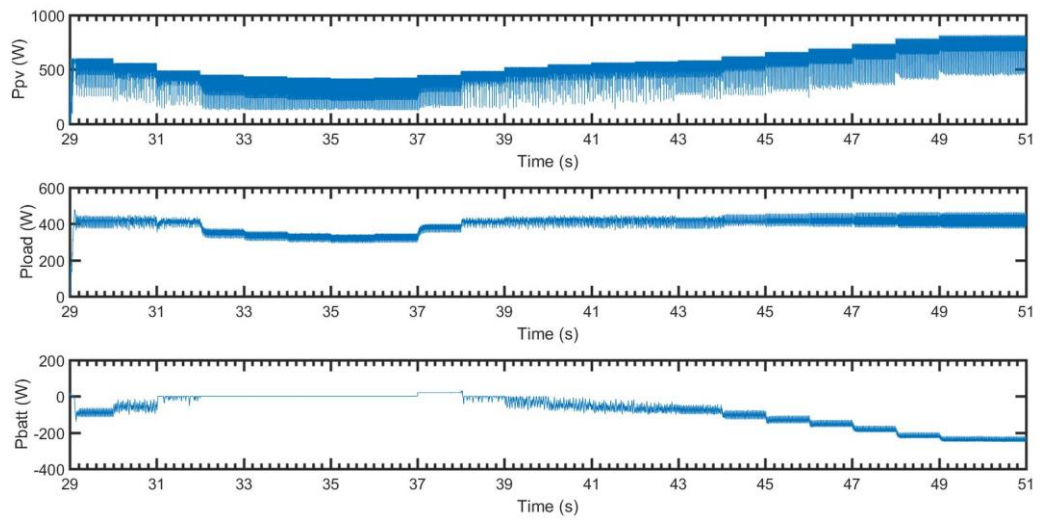


Figure 4-11 The power change of PV panels, load and battery (prediction horizon time: 5s)

Chapter 5 Summary and discussion

This research can be divided into two parts, the prediction of the solar irradiance/power and the control algorithm which uses this prediction for power dispatching strategy in advance.

5.1 Summary and prospective of the prediction method

In this work we used observations from an urban solar network based in Canberra, Australia, with the aim to predict both solar irradiance and solar power at a (generic) target station. Our target station, Namadgi School, is located in between, and at a few tens of kilometres from, two other monitoring stations, Black Mountain and Wombat Hill. All three stations, therefore including Namadgi School, have been collecting meteorological and power observations: this allows us to assess the predictions' performance at the target station. The sensitivity of two statistical methods, random forest and multi-linear, for i) different meteorological and power variables as predictors, ii) different combinations of stations, iii) winter and summer seasons and iv) different sky conditions, is an integral part of this work.

A number of variables observed at our monitoring stations were selected as our predictors for the GHI prediction – two global irradiances (GHI and on the plane of the PV panels), temperature, pressure and humidity. Clear sky radiation was also used as an additional predictor. Aside from the importance of historical values of GHI, the other important predictors are air temperature and humidity in summer and pressure and humidity in winter. As a benchmark for the GHI prediction, a modified (or gap) persistence, whereby

GHI values were simply modified by adding the next time step increment provided by the diurnal cycle (clear sky radiation), was used.

Compared to when only data from the two stations, Black Mountain and Wombat Hill, are used for GHI prediction, gap persistence yields better results for up to about 15 minutes ahead in summer. However, this clearly implies availability of data at the target station. Of the two statistical models, random forest is more skilful than the linear method in summer. In winter, gap persistence performs considerably better than for summer, with relative mean absolute errors (rMAEs) smaller than the two statistical methods out to about 60 minutes. Also, in winter the performance of the two statistical methods is reversed compared to summer, with the multi-linear method superior to random forest. The fact that the performance of these two methods displays a strong seasonality is a reflection of the prevalent climate conditions in Canberra in the two seasons. In winter, when clear sky conditions dominate, solar irradiance is better predicted by a less elaborate multi-linear method, whereas in variable, non-linear summer conditions the random forest method captures the GHI variability better.

For power output prediction, geometry and other specifications of the PV systems also play important roles, particularly at short lead times. This is because the local real-time tilted solar irradiance is roughly proportional to the real-time power output from solar panels (regardless of the negative efficiency effect due to increasing solar panel temperature). However, as the lead-time becomes longer, the positive effect of tilted solar irradiance as a predictor diminishes. Thus choosing GHI as a predictor instead of the solar irradiance on tilted surface when local data is not used seems to be acceptable as GHI is

less site-specific. As for other variables such as solar panels temperature, which in principle could be an important variable as it influences the solar panels' efficiency, in practice it did not make a marked impact on the power prediction accuracy.

In terms of the relative importance of stations, Black Mountain typically has a larger impact on the accuracy of GHI than Wombat Hill. However, for power prediction in summer the reverse seems to be true. These differences are mainly driven by dominant meteorological conditions. While the Canberra area is dominated by north-westerly winds, thus making Black Mountain more important for Namadgi School, in summer there is a pronounced occurrence of south-easterlies, due to the effect of sea breezes, which increases the importance of Wombat Hill in this season. In general, using both stations yields better results than using either one of them. Overall, stations representing dominant meteorological conditions appear to be the most effective at improving the forecast at the target station. Cloud movement is the biggest reason which influences how solar irradiance change. Therefore, the historical data from stations at upwind positions (stations representing dominant meteorological conditions) is more correlated to the real-time data of stations at downwind positions. The precise number of stations should be assessed on a case-by-case basis, namely by estimating the gain due to the marginal increase in accuracy for a specific application and the cost of setting-up and maintaining new stations.

In terms of predicting power output for a single site, global irradiance on tilted surface should be selected as a predictor if available. However, as this variable is site-specific, we demonstrated that by deriving it via a GHI conversion, with GHI observations at remote sites, a satisfactory prediction performance is obtained. Also, the prediction accuracy is higher under high clear-sky index conditions. This is especially the case in winter.

Possible future developments of the prediction work, aimed at improving the prediction accuracy, may be:

- The use of a predictor obtained from sky camera images; this would be most useful to improve predictions at the short range, up to about 20-30 minutes;
- The use of additional predictors such as a variable turbidity index;
- The use of a number of predictors from Numerical Weather Prediction output; these would be useful to improve the longer range, say 2-3 hours (and beyond), prediction skill;
- The use of a moving time window for the training period to continually update the parameters in the statistical model with more recent conditions. This would be particularly useful in an operational setting.

5.2 Summary and prospective of the control algorithm

In order to extract the maximum power from solar system, the PV panels are regulated by a unidirectional converter under MPPT (maximum power point tracking) algorithm. For the battery storage, the aim of the control algorithm is to balance the power generation (PV panels) and the consumption (Power loads) in the integrated PV and battery system. Battery is the device which is used to provide or absorb power when needed. Charging or discharging of the battery can be implemented by varying the battery terminal voltage. In this study, a simple battery model is used and if the battery terminal voltage is set over the predefined electromotive force (or the open circuit voltage of the battery), 50V, then it is charging. Otherwise, it is discharging (or be idle when the terminal voltage is exactly 50V). For the simple battery model, the charging and discharging power can be approximated by considering just the internal resistance and the battery voltage. As the internal

resistance is assumed to be constant, every reference value of battery power output corresponds to a particular reference value of battery voltage as shown in section 3.3.2.

One more thing that needs to be noted is that the references of the battery terminal voltage are simply calculated by considering the solar irradiance prediction and the power consumption. The absence of real-time measurements feedback/compensation mechanism means that the accuracy of future reference values highly relies on the accuracy of the prediction, which shows how prediction quality influence the overall system performance.

While the MPPT is relatively simple, this study focuses more on the MPC which is supposed to be a rolling window optimization control method. The controller can predict the values of different states and output 3 steps ahead based on the values (0 or 1) of the control signals. Result shows that when the prediction of solar irradiance changes dramatically, this controlling method can fulfil its function of balancing power and maintaining the voltage of DC bus within a certain range. However, there are also some potential improvements which can be implemented to make the controlling method more suitable for practical use:

- The battery system used in this study is a simplified one, so using a more complicated battery model can better represent a real battery system and improve the accuracy.
- Implement the control method on a physical prototype, which is a more straightforward way of checking the reliability and effectiveness of the algorithm.
- In this research, the state of charge of the battery is within the safe range. However, if the state of charge is over the maximum or below the minimum, an alternative control scheme should be used to guarantee system safety.

- Introduce a real-time measurement feedback/compensation mechanism involved in generating the references of battery terminal voltage. Though it is not implemented in this research with the aim of directly showing the connection between solar forecast quality and system performance, it will be a good way to improve the control quality of a practical system by setting a more reasonable reference trajectory.

References

1. Abdelsalam, A.K., et al., High-performance adaptive perturb and observe MPPT technique for photovoltaic-based microgrids. *IEEE Transactions on Power Electronics*, 2011. 26(4): p. 1010-1021.
2. Boland, J., Time-series analysis of climatic variables. *Solar Energy*, 1995. 55(5): p. 377-388.
3. Boland, J., L. Scott, and M. Luther, Modelling the diffuse fraction of global solar radiation on a horizontal surface. *Environmetrics*, 2001. 12(2): p. 103-116.
4. Breiman, L., Random forests. *Machine learning*, 2001. 45(1): p. 5-32.
5. Cutler, D.R., et al., Random forests for classification in ecology. *Ecology*, 2007. 88(11): p. 2783-2792.
6. Dincer, I., Renewable energy and sustainable development: a crucial review. *Renewable and Sustainable Energy Reviews*, 2000. 4(2): p. 157-175.
7. Elizondo, D., G. Hoogenboom, and R. McClendon, Development of a neural network model to predict daily solar radiation. *Agricultural and Forest Meteorology*, 1994. 71(1): p. 115-132.
8. Engerer, N. and F. Mills, K PV: A clear-sky index for photovoltaics. *Solar energy*, 2014. 105: p. 679-693.
9. Ernst, B., et al., Predicting the wind. *IEEE power and energy magazine*, 2007. 5(6): p. 78-89.
10. Esram, T. and P.L. Chapman, Comparison of photovoltaic array maximum power point tracking techniques. *IEEE Transactions on Energy Conversion EC*, 2007. 22(2): p. 439.
11. Femia, N., et al., Optimization of perturb and observe maximum power point tracking method. *IEEE transactions on power electronics*, 2005. 20(4): p. 963-973.
12. Golnas, A., et al. Performance assessment without pyranometers: predicting energy output based on historical Correlation. in *Photovoltaic Specialists Conference (PVSC), 2011 37th IEEE*. 2011. IEEE.
13. Hredzak, B. and V.G. Agelidis. Model predictive control of a hybrid battery-ultracapacitor power source. in *Power Electronics and Motion Control Conference (IPEMC), 2012 7th International*. 2012. IEEE.
14. Huang, J., et al., Forecasting solar radiation on an hourly time scale using a Coupled AutoRegressive and Dynamical System (CARDS) model. *Solar Energy*, 2013. 87: p. 136-149.
15. Ipakchi, A. and F. Albuyeh, Grid of the future. *IEEE Power and Energy Magazine*, 2009. 7(2): p. 52-62.
16. Ji, W. and K.C. Chee, Prediction of hourly solar radiation using a novel hybrid model of ARMA and TDNN. *Solar Energy*, 2011. 85(5): p. 808-817.
17. Karamanakos, P., T. Geyer, and S. Manias, Direct voltage control of DC-DC boost converters using enumeration-based model predictive control. *IEEE Transactions on Power Electronics*, 2014. 29(2): p. 968-978.

18. Khalid, M. and A. Savkin, A model predictive control approach to the problem of wind power smoothing with controlled battery storage. *Renewable Energy*, 2010. 35(7): p. 1520-1526.
19. Langley, P. and H.A. Simon, Applications of machine learning and rule induction. *Communications of the ACM*, 1995. 38(11): p. 54-64.
20. Li, X., D. Hui, and X. Lai, Battery energy storage station (BESS)-based smoothing control of photovoltaic (PV) and wind power generation fluctuations. *IEEE Transactions on Sustainable Energy*, 2013. 4(2): p. 464-473.
21. Liao, Z. and X. Ruan. A novel power management control strategy for stand-alone photovoltaic power system. in *Power Electronics and Motion Control Conference, 2009. IPEMC'09. IEEE 6th International. 2009. IEEE*.
22. Liaw, A. and M. Wiener, Classification and regression by randomForest. *R news*, 2002. 2(3): p. 18-22.
23. Lonij, V.P., et al. Forecasts of PV power output using power measurements of 80 residential PV installs. in *Photovoltaic Specialists Conference (PVSC), 2012 38th IEEE. 2012. IEEE*.
24. Lorenz, E., et al., Qualified Forecast of ensemble power production by spatially dispersed grid-connected PV systems. *Measurement*, 2007.
25. Lorenz, E., J. Kühnert, and D. Heinemann, Overview of irradiance and photovoltaic power prediction, in *Weather Matters for Energy*. 2014, Springer. p. 429-454.
26. Lorenz, E., et al., Regional PV power prediction for improved grid integration. *Progress in Photovoltaics: Research and Applications*, 2011. 19(7): p. 757-771.
27. Loutzenhiser, P., et al., Empirical validation of models to compute solar irradiance on inclined surfaces for building energy simulation. *Solar Energy*, 2007. 81(2): p. 254-267.
28. Mahmood, H., D. Michaelson, and J. Jiang. Control strategy for a standalone PV/battery hybrid system. in *IECON 2012-38th Annual Conference on IEEE Industrial Electronics Society. 2012. IEEE*.
29. Mohandes, M., S. Rehman, and T. Halawani, Estimation of global solar radiation using artificial neural networks. *Renewable Energy*, 1998. 14(1): p. 179-184.
30. Pirooz, A. and R. Noroozian. Model predictive control of classic bidirectional DC-DC converter for battery applications. in *Power Electronics and Drive Systems Technologies Conference (PEDSTC), 2016 7th. 2016. IEEE*.
31. Qi, W., et al., Supervisory predictive control of standalone wind/solar energy generation systems. *IEEE transactions on control systems technology*, 2011. 19(1): p. 199-207.
32. Rai, A.K., et al., Simulation model of ANN based maximum power point tracking controller for solar PV system. *Solar Energy Materials and Solar Cells*, 2011. 95(2): p. 773-778.
33. Raji, T., A. Boyo, and M. Hedayatshodeh, Analysis of global solar radiation data as time series data for some selected cities of western part of Nigeria. *International Journal of Advanced Renewable Energy Researches (IJARER)*, 2012. 1(1).

34. Reikard, G., Predicting solar radiation at high resolutions: A comparison of time series forecasts. *Solar Energy*, 2009. 83(3): p. 342-349.
35. Renné, D.S., Emerging meteorological requirements to support high penetrations of variable renewable energy sources: solar energy, in *Weather Matters for Energy*. 2014, Springer. p. 257-273.
36. Sharma, N., et al. Predicting solar generation from weather forecasts using machine learning. in *Smart Grid Communications (SmartGridComm)*, 2011 IEEE International Conference on. 2011. IEEE.
37. Solangi, K., et al., A review on global solar energy policy. *Renewable and sustainable energy reviews*, 2011. 15(4): p. 2149-2163.
38. Teleke, S., et al., Optimal control of battery energy storage for wind farm dispatching. *IEEE Transactions on Energy Conversion*, 2010. 25(3): p. 787-794.
39. Yang, D., P. Jirutitijaroen, and W.M. Walsh, Hourly solar irradiance time series forecasting using cloud cover index. *Solar Energy*, 2012. 86(12): p. 3531-3543.